Diverse densest binary sphere packings and phase diagram

Ryotaro Koshoji,[*] Mitsuaki Kawamura,[†] Masahiro Fukuda,[‡] and Taisuke Ozaki[§]
Institute for Solid State Physics, The University of Tokyo, Kashiwa 277-8581, Japan

(Received 14 October 2020; accepted 26 January 2021; published 19 February 2021)

We revisit the densest binary sphere packings (DBSPs) under periodic boundary conditions and present an updated phase diagram, including newly found 12 putative densest structures over the $x-\alpha$ plane, where x is the relative concentration and α is the radius ratio of the small and large spheres. To efficiently explore the DBSPs, we develop an unbiased random search approach based on both the piling-up method to generate initial structures in an unbiased way and the iterative balance method to optimize the volume of a unit cell while keeping the overlap of hard spheres minimized. With those two methods, we have discovered 12 putative DBSPs and thereby the phase diagram is updated, while our results are consistent with those of a previous study [Hopkins *et al.*, Phys. Rev. E **85**, 021130 (2012)] with a small correction for the case of 12 or fewer spheres in the unit cell. Five of the discovered 12 DBSPs are identified in the small radius range of $0.42 \leqslant \alpha \leqslant 0.50$, where several structures are competitive to each other with respect to packing fraction. Through the exhaustive search, diverse dense packings are discovered and, accordingly, we find that packing structures achieve high packing fractions by introducing distortion and/or combining a few local dense structural units. Furthermore, we investigate the correspondence of the DBSPs with crystals based on the space group. The result shows that many structural units in real crystals, e.g., LaH_{10} and $SrGe_{2-\delta}$ being high-pressure phases, can be understood as DBSPs. The correspondence implies that the densest sphere packings can be used effectively as structural prototypes for searching complex crystal structures, especially for high-pressure phases.

DOI: 10.1103/PhysRevE.103.023307

I. INTRODUCTION

The densest sphere packings can be used as structural models for many physical systems, e.g., crystals, colloids [1,2], and glasses [3]. Atoms in crystals are sometimes approximated as spheres: In ion-bonded materials such as NaCl [4], atoms are often spherically symmetrical because atoms have closed-shell structures due to the charge transfer. In intermetallic compounds such as AgCu [5], atoms are also sometimes spherically symmetrical due to the bonds formed by electrons populating in *s* orbitals. In materials under high pressure, distances between atoms become so close that the directional orientation of the bond is weakened due to the strong repulsive force by Pauli's exclusion principle [6]. Accordingly, many structural units in crystals can be understood as sphere packings [7]. The correspondences indicate that the densest sphere packings may be used effectively as structural prototypes for searching complex crystal structures, especially for high-pressure phases.

Identifying the densest sphere packings is one of the most difficult mathematical problems. It was proved only in the 2000s that the Barlow packing is the densest packing of monodisperse spheres in $\mathbb{R}^3$ [8]. There seems no general way to determine the densest binary sphere packings (DBSPs) in a mathematically rigorous way despite considerable efforts under limited conditions [9–11]. However, there have been several studies that attempt to estimate the DBSPs by numerical calculations [12–18]. Recently, Hopkins *et al.* explored the DBSPs under the restriction that the number of spheres in the unit cell is less than or equal to 12. They used the original method to generate initial structures [19] and structural optimization algorithms [20]. Accordingly, they constructed the phase diagram for DBSPs [21,22]; hereafter, we call the diagram the HST phase diagram. Eighteen distinct putative DBSPs were identified on the HST phase diagram. The phase diagram for the densest ternary sphere packings has not yet been constructed.

An exhaustive search for packing structures becomes more difficult with an increase in the number of spheres. The considerable increase in the number of local minima is inferred from the explosive increase in the number of permutations of lining up spheres in a row. The number of cases with six large and six small spheres is 924, whereas the number of cases with 12 large and 12 small spheres is 2 704 156. In general, the number of cases R with N large and N small spheres can be calculated as

$$R = \frac{(2N)!}{N!N!}. \tag{1}$$

With Stirling's formula, R can be estimated as

$$R \sim \frac{4^N}{\sqrt{\pi N}}. \tag{2}$$

[*]cosaji@issp.u-tokyo.ac.jp
[†]mkawamura@issp.u-tokyo.ac.jp
[‡]masahiro.fukuda@issp.u-tokyo.ac.jp
[§]t-ozaki@issp.u-tokyo.ac.jp

Equation (2) indicates that the number of local minima in three-dimensional structures is getting larger exponentially with an increase in the number of spheres.

Prediction of crystal structures faces the same difficulties. Many algorithms to explore effectively in coordination spaces have been devised for crystal structure prediction, e.g., the evolutionary algorithm [23–27] and the particle-swarm optimization method [28–31]. It is also known that symmetry constraints enhance the efficiency of finding the most stable structure [27–29,31]. Those methods have successfully predicted many materials, followed by experimental confirmations [23–32].

The random structure searching method [33] is also a powerful method for structure prediction. We consider that the densest sphere packings should be searched by the random structure searching method because we have no *a priori* knowledge about what kinds of structures are the densest multinary sphere packings. For example, the densest structures may not be highly symmetric; therefore, those structures may not be found under symmetry constraints. On the other hand, the random structure searching method has a drawback that it is impossible to explore exhaustively in coordination space unless structural optimization is efficient. However, in the case of hard spheres, structural optimization is expected to be efficient because repulsive forces occur only when two spheres overlap each other. Therefore, the random structure searching method is to be regarded as an effective way to search for the densest packings.

In the present research, we revisit the DBSPs under periodic boundary conditions. To efficiently explore the densest sphere packings, first we invent the *piling-up method* to generate initial structures in an unbiased way; second, we develop the *iterative balance method* to optimize the volume of a unit cell while keeping the overlap of hard spheres minimized. The piling-up method is developed based on the idea of stacking spheres randomly one by one on top of a randomly generated first layer. It enables us to search the densest packings unbiasedly from the vast coordination space. The iterative balance method is developed based on the idea of repeating collision and repulsion among spheres under pressure while the maximum displacement in position vectors and lattice vectors is gradually decreased. The method not only generates a dense, periodic packing of nonoverlapping spheres but also predicts the maximum packing fraction with high accuracy. Those two methods are implemented in our open-source program package SAMLAI (Structure search Alchemy for MateriaL Artificial Invention). With SAMLAI, we exhaustively search the DBSPs with extending the unit cell compared to the previous study [22] and, as a result, we update the phase diagram, including discovered 12 putative DBSPs over the $x-\alpha$ plane, where x is the relative concentration and α is the radius ratio of the small and large spheres. x is defined as

$$x \equiv \frac{s}{S+s}, \tag{3}$$

where S (s) is the number of large (small) spheres in the unit cell. For the case of 12 or fewer spheres in the unit cell, our phase diagram is consistent with that of a previous study [22] with a small correction. Through the exhaustive search, diverse monophase DBSPs are discovered; accordingly, we find that high packing fractions are achieved by introducing distortion and/or combining a few local dense structural units. Furthermore, we investigate the correspondence of the DBSPs with crystals based on the space group. The result shows that many structural units in real crystals, e.g., LaH_{10} [34] and $SrGe_{2-\delta}$ [35] synthesized under high pressure, can be understood as DBSPs. The correspondence implies that the densest sphere packings can be used effectively as structural prototypes for searching complex crystal structures, especially for high-pressure phases.

The paper is organized as follows: Section II describes our method to explore the densest sphere packings; Sec. III discusses the numerical aspects of our method, e.g., the accuracy of the packing fraction and the distribution of generated packing fractions; Sec. IV details the methodology for constructing the phase diagram for DBSPs; Sec. V presents the phase diagram and discovered 12 putative DBSPs; Sec. VI discusses the effectiveness of our method and the geometry of DBSPs. In Sec. VII, we summarize this study.

II. OUR IMPLEMENTATION

To efficiently explore the densest packings, we develop an unbiased random search method. The method is implemented in our open-source program package SAMLAI. It consists of two steps: (A) random generation of multi-layered structures and (B) structural optimization. Step A is aimed at generating initial structures and step B is aimed at optimizing the initial structures for high packing fractions.

A. Generation of initial structures: *Piling-up method*

As discussed by Pickard and Needs [33], randomly generated structures may contain spheres that are very close together or spheres may be crowded in a direction of a short lattice vector instead of a long lattice vector. To avoid generating such an abnormal initial structure, we develop the *piling-up method* to randomly generate appropriate initial structures. The method is based on an idea of stacking spheres randomly one by one on top of a randomly generated first layer, since any periodic structure can be understood as a multilayered structure if it is extended in a direction perpendicular to a chosen base plane.

The piling-up method consists of two steps. First, an initial structure is generated randomly. Next, a multilayered structure is constructed by expanding an initial structure.

1. Generation of seed structure

To generate an initial structure, first a large sphere is placed at $(0, 0, 0)$. Hereafter, the position of sphere (q_{i1}, q_{i2}, q_{i3}) is represented in the fractional coordinates and the maximum radius of spheres is set to 1. All values we discuss in the paper are dimensionless. The initial lattice vectors are set to

$$\boldsymbol{a}_1 = (a_{11}, 0, 0), \tag{4}$$

$$\boldsymbol{a}_2 = (a_{21}, a_{22}, 0), \tag{5}$$

$$\boldsymbol{a}_3 = (a_{31}, a_{32}, a_{33}), \tag{6}$$

where we set $a_{11} = 2$ and $a_{22} = 2$; the a_{21} is set to a random value in the range of $-1 \leqslant a_{21} < 1$ to allow $\boldsymbol{a}_2$ to have

freedom of angle of 60° to 120° relative to $\boldsymbol{a}_1$. Next, zero or more spheres are randomly selected to place on the first layer spanned by $\boldsymbol{a}_1$ and $\boldsymbol{a}_2$. The selected spheres are placed at $(r, r', 0)$, where r and r' are random values in the range of $0 \leqslant r, r' < 1$. These operations correspond to the random generation of the first layer. The initial lattice vectors have a very strong restriction as $a_{11} = a_{22}$; furthermore, there can be a large overlap between spheres placed on the first layer. However, as discussed in the next subsection, these structural features can be relaxed simultaneously by expanding the unit cell with the steepest descent method. At this stage, we do not expand the cell, but continue to generate the initial structure.

Next, the unselected spheres are stacked one by one. As the first step in the second stage, $\boldsymbol{a}_3$ is set to

$$\boldsymbol{a}_3 = r\boldsymbol{a}_1 + r'\boldsymbol{a}_2 + (0, 0, a_{33}), \tag{7}$$

where r and r' are random values in the range of $-0.5 \leqslant r, r' < 0.5$; a_{33} is set to

$$a_{33} = \sum_I c_I + 1, \tag{8}$$

where c_i is defined as the radius of the sphere i and I is the labels of unselected spheres. Finally, all unselected spheres are picked up one by one and they are placed at (r, r', q_{i3}) where r and r' are random values within $0 \leqslant r, r' < 1$ and the q_{i3} is set so the z coordinate will be increased by the radius of the sphere to be placed every time a sphere is placed.

2. Expansion

The generated unit cell seems to be very biased and generally there can be a large overlap between spheres. If we simply scale the unit cell so the largest overlap can become zero, the cell may expand explosively and the initial constraint of $a_{11} = a_{22}$ would nearly hold. However, if the initial structure is expanded with the steepest descent method, the lattice vectors are adjusted to the optimal length and angle, depending on the sphere arrangement. For example, if many spheres are piled up in a particular direction, the lattice vectors are greatly expanded in that direction.

To apply the steepest descent method for the expansion, we introduce a two body interaction potential between spheres $U(|\boldsymbol{r}_j + \boldsymbol{T} - \boldsymbol{r}_i|)$, where $\boldsymbol{r}_i$ is the position of sphere i and $\boldsymbol{T}$ is the translational lattice vector. We also define the total energy E per unit cell as

$$E = \frac{1}{2} \sum_{\boldsymbol{T}} \sum_{i=1}^{N} \sum_{j=1}^{N} U(|\boldsymbol{r}_j + \boldsymbol{T} - \boldsymbol{r}_i|), \tag{9}$$

where N is the number of spheres in the unit cell. The two body interaction potential $U(|\boldsymbol{r}_j + \boldsymbol{T} - \boldsymbol{r}_i|)$ is defined to be

$$U(|\boldsymbol{r}_j + \boldsymbol{T} - \boldsymbol{r}_i|) \equiv \begin{cases} -z_{ij}^{(\boldsymbol{T})} & z_{ij}^{(\boldsymbol{T})} \leqslant 0 \\ 0 & 0 < z_{ij}^{(\boldsymbol{T})}, \end{cases} \tag{10}$$

with

$$z_{ij}^{(\boldsymbol{T})} \equiv |\boldsymbol{r}_j + \boldsymbol{T} - \boldsymbol{r}_i| - (c_i + c_j), \tag{11}$$

where c_i is the radius of sphere i. The characteristic features of the potential are two folds: one is that the potential is nonzero only when two spheres overlap with each other, and the other is that the repulsive force is constant when overlapping. If the potential $U(|\boldsymbol{r}_j + \boldsymbol{T} - \boldsymbol{r}_i|)$ is smoothly connected with $z_{ij}^{(\boldsymbol{T})} = 0$, it becomes a pseudo-hard-sphere potential. The smoothness causes an undesirable overlap between spheres when a finite pressure is applied to increase the packing fraction, as discussed later.

To expand the unit cell, the extended coordinates defined with

$$\boldsymbol{u} \equiv (q_{11}, q_{12}, q_{13} \cdots q_{N3}, a_{11}, a_{12}, a_{13}, \cdots a_{33}) \tag{12}$$

is updated by the steepest descent method as

$$\Delta\boldsymbol{u} = -k_1 \frac{\partial E}{\partial \boldsymbol{u}}, \tag{13}$$

where k_1 is the steepest descent prefactor. The steepest descent method is repeated until the size of the gradient is less than a threshold value. As a result, a multilayered structure is generated. We calculate the derivatives analytically in Appendix C.

If the size of the gradient is more than a threshold value, $\Delta\boldsymbol{u}$ is scaled so the maximum displacement in the position vectors and lattice vectors will be equal to the predetermined value. The prefactor k_1 is not set directly. The expansion step is not aimed at optimizing structures but producing diverse multilayered structures. Therefore, it makes sense to scale $\Delta\boldsymbol{u}$ to an optimal size that is neither too large nor too small. The value of the maximum displacement is presented in Sec. III A.

The piling-up method is able to create diverse multilayered structures with appropriate lattice vectors depending on the sphere arrangement. With the iterative balance method discussed in Sec. II C, the generated structures can be optimized to diverse packing structures, e.g., towerlike structures and symmetric structures such as the fcc structure. The piling-up method is very effective for searching densest sphere packings, as discussed in Sec. III F.

B. Global optimization

The generated multilayered structure contains a large gap, which makes the packing fraction reduced. The large gap can be filled by steepest descent method under pressure with the hard-sphere potential defined as Eq. (10), since the method can cause a repetition of collision and repulsion between spheres. If the constant repulsive force is large enough, it never balances with the pressure. The repulsion is dominant when overlapping, leading to a structure without any overlap as a result of the optimization. Once the optimization reaches a structure without any overlap, the pressure is only the driving force to change the structure because of the characteristic feature of the two-body interaction defined by Eq. (10), and the optimization leads to a structure with overlap again. This means that the optimization cannot finish, but enables collision and repulsion between spheres to be repeated as long as we continue. The pressure is necessary to minimize the volume of the unit cell. In each steepest descent step, the extended coordinates $\boldsymbol{u}$ is changed to minimize the enthalpy per unit cell H as

$$\Delta\boldsymbol{u} = -k_2 \frac{\partial H}{\partial \boldsymbol{u}}, \tag{14}$$

where k_2 is the steepest descent prefactor and the enthalpy is defined as $H \equiv E + PV$; P is the pressure and V is the volume of the unit cell. The operation is not aimed at converging the enthalpy to a local minimum but transforming significantly an initial structure to a dense structure with a large number of the repetition of collision and repulsion. A lot of iteration is essential for sufficient structural transformation. In fact, we have confirmed that the linear minimization method does not work. In the global optimization step, the steepest descent method is repeated several thousand times.

Since the forces and the pressure are never balanced, any structure can transform into a dense structure. The effectiveness comes from the hard-sphere potential defined as Eq. (10).

As with the expansion process discussed before, the steepest descent prefactor k_2 is not set directly, but $\Delta \boldsymbol{u}$ is scaled so the maximum displacement in the position vectors and the lattice vectors will be equal to the predetermined value. The purpose of the global optimization is only to fill the wasteful gaps, so it is the most important how much the position vectors and lattice vectors are allowed to displace. Setting the maximum displacement has the advantage of allowing each sphere to move enough even when the number of spheres in the unit cell is large. Therefore, it makes sense to set $\Delta \boldsymbol{u}$ to an appropriate size so the wasted gaps can be filled. During the global optimization, the maximum displacement is kept constant. The pressure P is also kept constant as $P = 0.1$. The other values are presented in Sec. III A.

Even after a large number of optimization steps, the overlap never converges to zero, because $z_{ij}^{(\boldsymbol{T})}$ between neighboring spheres oscillate around zero. The overlap converges to zero with the local optimization, which we discuss next.

C. Local optimization: *Iterative balance method*

To optimize a structure to a periodic packing of nonoverlapping spheres, all the overlaps have to be converged to zero. In other words, all of the $z_{ij}^{(\boldsymbol{T})}$ have to be converged to more than or equal to zero. To achieve the condition, we develop the *iterative balance method*. The iterative balance method optimizes the volume of a unit cell while keeping the overlap of hard spheres minimized. The method is developed based on the idea of repeating collision and repulsion among spheres under pressure while the maximum displacement in position vectors and lattice vectors is gradually decreased. The pressure P is kept constant as $P = 0.1$ through the iterative balance method.

In the iterative balance method, collision and repulsion between spheres are also repeated with the steepest descent method. As with the global optimization, the steepest descent prefactor k_2 is not set directly, but $\Delta \boldsymbol{u}$ is scaled so the largest displacement in the position vectors and lattice vectors will be equal to a certain value. To converge all of $z_{ij}^{(\boldsymbol{T})}$ to more than or equal to zero, the maximum displacement is gradually decreased for each step.

To illustrate the convergence of $z_{ij}^{(\boldsymbol{T})}$, we consider the structural optimization in the one-dimensional case. Here, as shown in Fig. 1, we assume that two spheres interact with the

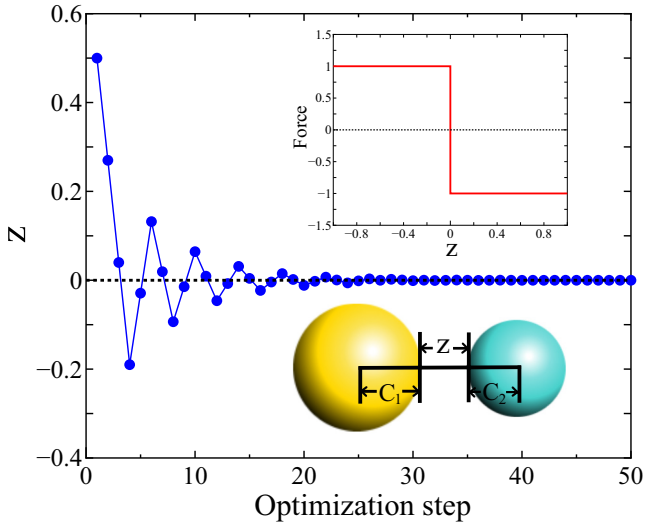

FIG. 1. The iterative balance method in the one-dimensional case. Two spheres interact with the discontinuous force. With decrease in the displacement, z eventually converges to zero.

discontinuous force defined to be

$$f = \begin{cases} 1 & z \leqslant 0 \\ -1 & 0 < z, \end{cases} \tag{15}$$

with

$$z \equiv r - (c_1 + c_2), \tag{16}$$

where r is the distance between the two spheres. If the model is optimized by the steepest descent method with a constant prefactor, z oscillates around $z = 0$, and never reaches $z = 0$. On the other hand, if the displacement is gradually reduced, z eventually converges to zero. The convergence behavior is shown in Fig. 1 together with the one-dimensional model and the discontinuous force defined by Eq. (15) as in the inset.

The idea works even for the three-dimensional case we are interested in. Once we control the prefactor so the maximum displacement can be gradually reduced, the structure eventually reaches a packing structure with almost zero overlaps. In this sense, $z_{ij}^{(\boldsymbol{T})} = 0$ can be regarded as a *balanced* point. This is the reason why we call it the iterative balance method. The size of the maximum displacement is the same order as the maximum overlap as discussed in Sec. III B, where the maximum overlap is defined to be the maximum value in $-z_{ij}^{(\boldsymbol{T})}$. It should be clearly noted that the discontinuous change of sign in forces produced by Eq. (10) is crucial to realize the balanced point. Other potentials such as the squared potential of z do not provide the interesting feature.

The iterative balance method can find the optimal distortion because the pressure makes as many $z_{ij}^{(\boldsymbol{T})}$ converge to zero as possible. That distortion is exactly what makes it possible to minimize the volume of the unit cell. The feature indicates that the iterative balance method can find the local maximum of packing fractions, despite the fact that a large number of optimization steps is necessary to find the maximum packing fraction. The optimization parameters such as the optimization step number are presented in Sec. III A.

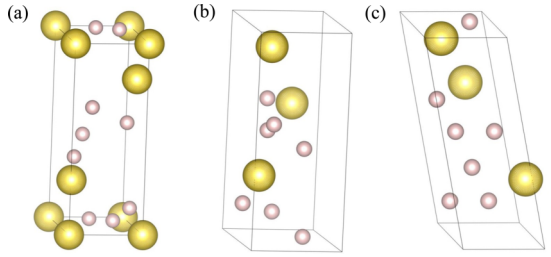

FIG. 2. Generation process of the (7-3) structure [22]. (a) Generation of a seed structure by piling-up method. (b) Expansion of the seed structure by steepest descent method. (c) The final structure obtained by iterative balance method. The bottom side is narrow and the vertical direction is long. The feature corresponds to that of the seed structure. Figures are generated by VESTA [36].

Just like the Torquato-Jiao sphere-packing algorithm [20], in principle the iterative balance method allows us to evaluate the packing fraction of the dense sphere packings while avoiding overlaps of spheres. The implementation is straightforward and the computational time for the structural optimization is very short, as discussed later on, since it requires only simple calculations of forces and stress at each steepest descent step. We will demonstrate the efficiency and ability to find the putative densest structures in Sec. III.

D. Examples of structure generation

The (7-3) structure [22] is the towerlike DBSP with seven small and three large spheres in the unit cell. The formation process of the structure is shown in Fig. 2. First, the towerlike structure is generated by stacking many spheres on top of the small bottom plane as shown in Fig. 2(a), and then the structure is expanded as shown in Fig. 2(b) with the steepest descent method. The bottom plane corresponds to the first layer generated by piling-up method. The final structure, shown in Fig. 2(c), also has a small bottom plane and is long in the vertical direction.

The (16-4) structure is the DBSP with 16 small and four large spheres in the unit cell. The structure can be understood as a two-layered structure except for four small spheres. The formation process of the structure is shown in Fig. 3. For visibility of the figures, the bottom plane, which is the first layer generated by piling-up method, is arranged at the front side. First, all the spheres are placed on the first layer as shown in Fig. 3(a), and then the structure is expanded as shown in Fig. 3(b). The final structure, shown in Fig. 3(c), can also be regarded as a layer-by-layer structure with a small height.

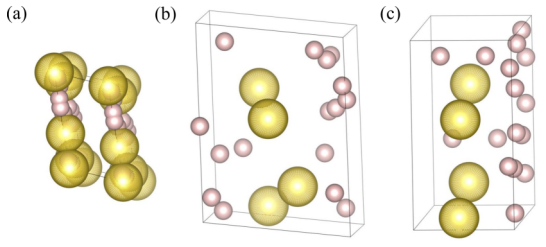

FIG. 3. Generation process of the (16-4) structure. For visibility of the figures, the bottom side, which is the first layer generated by piling-up method, is arranged at the front side. (a) Generation of a seed structure by piling-up method, where all the spheres are placed in the first layer. (b) Expansion of the seed structure by steepest descent method. (c) The final structure obtained by iterative balance method.

E. Neighboring spheres

In the optimization process, if a packing structure sufficiently converges to a dense structure, almost all the position vectors do not displace significantly even after many optimization steps. In addition, repulsive forces occur only when two spheres overlap each other. Therefore, the computational cost can be reduced significantly by predetermining the neighboring spheres. Of course, we must reset the neighboring list periodically because, accidentally, position vectors may displace largely. In our code, the neighboring list is reset once every 100 times in the global optimization step and once every 200 times in the local optimization step.

F. Treatment of similar initial multilayer structures

First, we define the word isomorphic: We regard two structures as isomorphic if the two structures are identical when the Cartesian coordinates for one of them are displaced by a small threshold value, where we select the threshold value within a range so the change of the packing fraction can be less than 0.001. Unit cells are not necessarily the same. The variation of packing fractions comes from the difference of distortions. Distortion is necessary to achieve a high packing fraction.

One may consider that it is futile to optimize all similar structures which converge to an isomorphic structure. However, in some cases, the number of local minima of the enthalpy is huge due to a large number of distortion patterns and, accordingly, many structures are trapped at local minima. Therefore, optimizing all similar structures is necessary to determine the highest packing fraction. Hence, we optimize all generated structures.

III. NUMERIC ASPECT OF OUR METHOD

In this section, we discuss the numerical aspects of our method, including structural optimization parameters, accuracy of the packing fraction, and efficiency of our method.

A. Optimization parameters for exhaustive search

The efficiency of structural optimization depends on the choice of parameters used in the optimization, and even the reachable maximum packing fraction is varied, depending on the parameters, in case many local minima have competitive packing fractions. These parameters we have are listed below:

(1) $\Delta_{\mathrm{expand,max}}$: The maximum displacement in the expansion step

(2) $\Delta_{\mathrm{global,max}}$: The maximum displacement in the global optimization step

(3) N_{global}: The iteration number in the global optimization step

(4) $\Delta_{\mathrm{local,max}}$: The maximum displacement in the local optimization step

TABLE I. Default values of optimization parameters. For each optimization process, $\Delta_{\mathrm{global,max}}$ and $\Delta_{\mathrm{local,max}}$ are determined randomly from the range shown in the table. Each parameter is defined in Sec. III A.

Optimization parameter	Default value for exhaustive search	Default value for high-precision optimization
$\Delta_{\mathrm{expand,max}}$	0.3	–
$\Delta_{\mathrm{global,max}}$	$0.03 \leqslant \Delta_{\mathrm{global,max}} \leqslant 0.15$	$0.003 \leqslant \Delta_{\mathrm{global,max}} \leqslant 0.05$
N_{global}	2000	4000
$\Delta_{\mathrm{local,max}}$	$0.02 \leqslant \Delta_{\mathrm{local,max}} \leqslant 0.10$	$0.001 \leqslant \Delta_{\mathrm{local,max}} \leqslant 0.02$
N_{local}	40000	80000
d	0.9997	0.9997

(5) N_{local}: The iteration number in the local optimization step

(6) d: The decreasing factor of the maximum displacement in the local optimization step

The default values for exhaustive search are given in Table I. Here, we note that $\Delta_{\mathrm{global,max}}$ ($\Delta_{\mathrm{local,max}}$) is chosen randomly in the range of $0.03 \leqslant \Delta_{\mathrm{global,max}} \leqslant 0.15$ ($0.02 \leqslant \Delta_{\mathrm{local,max}} \leqslant 0.05$) for each structural optimization, as written in Table I. The random choice of them enables us to obtain various local minima. The default parameters lead to a convergence that almost all the minimum value of $z_{ij}^{(\boldsymbol{T})}$ becomes the same order as -10^{-7} to -10^{-6}.

B. Maximum overlap

In the iterative balance method, the maximum displacement of the position vectors and the lattice vectors are gradually reduced. Figure 4 shows the maximum overlaps at each optimization step. $\Delta_{\mathrm{local,max}}$ is set to 0.0546375. The maximum overlap is defined as the maximum value of $-z_{ij}^{(\boldsymbol{T})}$. It is confirmed from Fig. 4 that the maximum overlap decreases exponentially as the maximum displacement is decreased exponentially, and those values are the same order. The relation can be understood from the fact that some of $z_{ij}^{(\boldsymbol{T})}$ between neighboring spheres oscillate around zero.

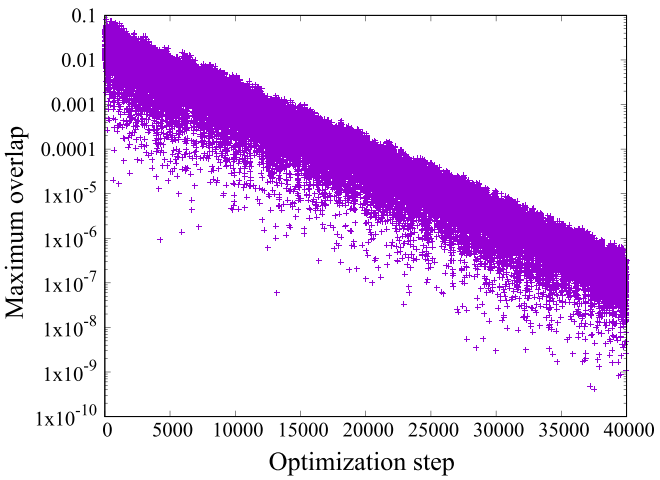

FIG. 4. The maximum overlap at each optimization step where the maximum overlap is defined as the maximum value of $-z_{ij}^{(\boldsymbol{T})}$. The maximum overlap decreases exponentially as the maximum displacement is decreased exponentially.

C. Accuracy of packing fraction

In the radius ratio of $\alpha \leqslant \sqrt{2}-1$, the $\mathrm{XY_n}$ structures appear on the phase diagram. The $\mathrm{XY_n}$ structures are defined as packing structures in which large spheres X constitute the fcc densest structure and small spheres Y penetrate into the tetrahedral and octahedral sites constituted by X. The packing fractions of the $\mathrm{XY_n}$ structures can be calculated analytically as

$$\phi = \frac{\pi}{3\sqrt{2}}(1+n\alpha^3). \tag{17}$$

In the radius ratio of $\alpha \leqslant \sqrt{2}-1$, as discussed by Hopkins *et al.*, six $\mathrm{XY_n}$ structures of XY, $\mathrm{XY_2}$, $\mathrm{XY_4}$, $\mathrm{XY_8}$, $\mathrm{XY_{10}}$, and $\mathrm{XY_{11}}$ [22] appear on the phase diagram. An octahedral site of XY structure is occupied by one small sphere, an octahedral site of $\mathrm{XY_2}$ structure is occupied by two small spheres, an octahedral site of $\mathrm{XY_4}$ structure is occupied by a tetrahedron consisting of four small spheres, an octahedral site of $\mathrm{XY_8}$ is occupied by a cubic consisting of eight small spheres, a tetrahedral site of $\mathrm{XY_{10}}$ structure is occupied by one small sphere and an octahedral site of $\mathrm{XY_{10}}$ is occupied by a cubic consisting of eight small spheres, and a tetrahedral site of $\mathrm{XY_{11}}$ structure is occupied by one small sphere and an octahedral site of $\mathrm{XY_{11}}$ is occupied by a bcc structure consisting of nine small spheres, respectively.

It was relatively easy to calculate the packing fractions of the $\mathrm{XY_n}$ structures with our method because there is no distortion in the fcc structure constituted by large spheres. However, when the optimization parameters are set to the default values, in some cases an error of the packing fraction becomes the same order as 10^{-6} due to overlap, which is also the same order as 10^{-6}. As discussed in the next section, by optimizing again with changing the optimization parameters, the maximum overlap can be decreased to the same order as 10^{-13}. In that case, the packing fractions agree by more than ten decimal points with the analytical solution of Eq. (17).

As discussed in Sec. II C, the iterative balance method can minimize the volume of a unit cell. Therefore, high-precision reoptimization enables us to find the highest packing fractions with high accuracy because of a small overlap and a minimized volume of a unit cell.

D. High-precision structural optimization

As discussed in Sec. III C, the local optimization with default values for exhaustive search presented in Table I cannot reduce an overlap enough. The overlap causes an error in the packing fraction after the six decimal points. The error can be

reduced by a high-precision reoptimization. With an increase in the number of local optimization steps, the overlap can be decreased because the maximum displacement is decreased as the number of optimization steps is increased. As discussed in Sec. III B, the maximum overlap and the size of the maximum displacement is the same order.

When the number of local minima is getting larger, more structures are trapped at local minima, so the global minimum might not be found during an exhaustive search. Therefore, it is necessary to reoptimize the putative densest structure many times to identify the global minimum. The optimization results depend on the initial structure and the optimization parameters, such as $\Delta_{\mathrm{global,max}}$ and $\Delta_{\mathrm{local,max}}$. Therefore, slight fluctuations are given to the structure before reoptimization and the range of $\Delta_{\mathrm{global,max}}$ and $\Delta_{\mathrm{local,max}}$ is set to be large. When the number of local minima is small, almost all the fluctuated structures converge to the densest packing. On the other hand, when the number of local minima is large, we obtain many packing fractions corresponding to diverse distortion patterns. In some cases, tens of thousands of reoptimizations are necessary to determine the maximum packing fraction. As discussed in the next subsection, the computational time for the structural optimization is very short, so the necessity of the several thousand reoptimizations is not a serious problem.

The default parameters for reoptimization are given in Table I. If we use the default parameters, in almost all cases, the minimum values of $z_{ij}^{(T)}$ become the same order as -10^{-13} to -10^{-12}.

E. Speed of structure generation

The computational cost for calculating forces with the hard-sphere potential is very low because repulsive forces occur only when two spheres overlap each other. In addition, if a packing structure converges to a dense packing, the positions of the spheres do not change significantly even after many optimization steps. Therefore, as discussed in Sec. II E, the computational cost can be significantly reduced by predetermining the neighboring spheres. In fact, if the number of spheres in the unit cell is about ten, it takes less than 0.1 seconds from generation to optimization using a single core of Intel(R) Xeon(R) CPU E5-1650 v4 @ 3.60 GHz. Therefore, our method can generate a large number of packing structures. The efficiency enables us to find the densest packing from the vast coordination space.

In addition, since the number of optimization steps is set externally, the computational cost can be estimated as $O(N)$, where N is the number of spheres. Hence, it is possible to conduct an exhaustive search for the long periodic densest packings.

F. Distribution and update history of packing fractions

In this subsection, we discuss the distribution and updating history of packing fractions during the exhaustive search, to show that our method can find the densest packings from the vast coordination space.

First, we conducted an exhaustive search for the monophase DBSPs at the radius ratio of $\alpha = 0.445$ and the composition ratio of $x = 14/19$. The unit cell contains 14 small spheres and five large spheres. In that case, the (14-5) structure with the packing fraction of 0.765259 is the densest. The number of structures generated during the exhaustive search is 250 182. The distribution of the packing fractions is shown in Fig. 5(a). The number of structures having a packing fraction between 0.6875 and 0.6900 is 15959 and the largest. On the other hand, the number of structures having a packing fraction between 0.7650 and 0.7675 is only 58. The result indicates that our method can find the densest packings from the vast coordination space. Figure 6(a) shows the updating history of the highest packing fraction. The structure with a packing fraction of 0.765256 is generated at the 9372nd step, while the densest structure with the packing fraction of 0.765259 is generated at the 50 155th step.

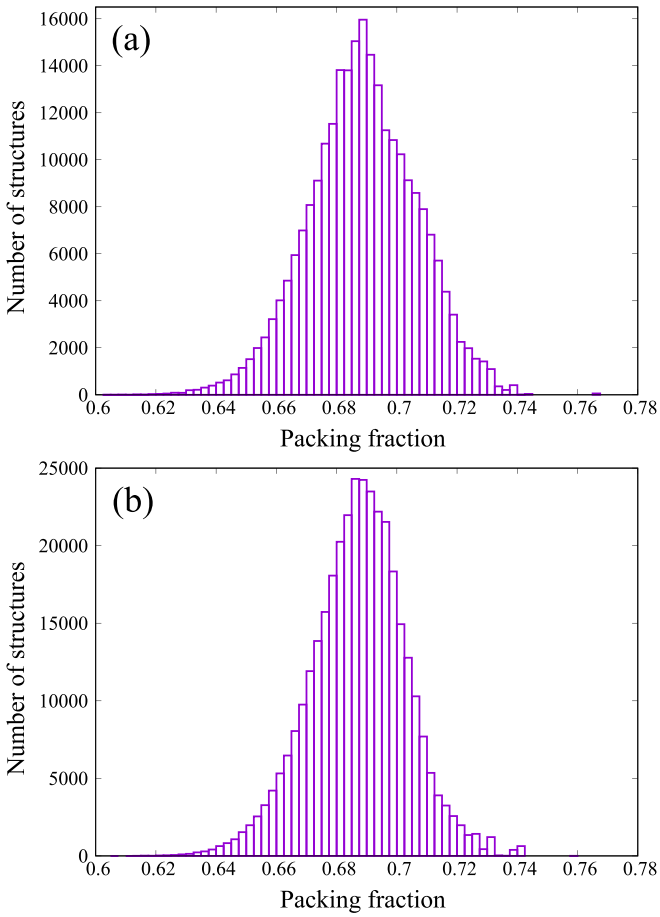

FIG. 5. The distribution of the packing fractions during the exhaustive search. (a) The distribution for 14-5 system; the unit cell contains 14 small spheres and five large spheres. The radius ratio is $\alpha = 0.445$. (b) The distribution for 16-4 system; the unit cell contains 16 small spheres and four large spheres. The radius ratio is $\alpha = 0.455$.

Similarly, we conducted an exhaustive search for the monophase DBSP at the radius ratio of $\alpha = 0.455$ and the composition ratio of $x = 16/20$. The unit cell contains 16 small spheres and four large spheres. In that case, the (16-4) structure with the packing fraction of 0.759629 is the densest. The number of structures generated during the exhaustive search is 351 124. The distribution of the packing fractions is shown in Fig. 5(b). The number of structures having the

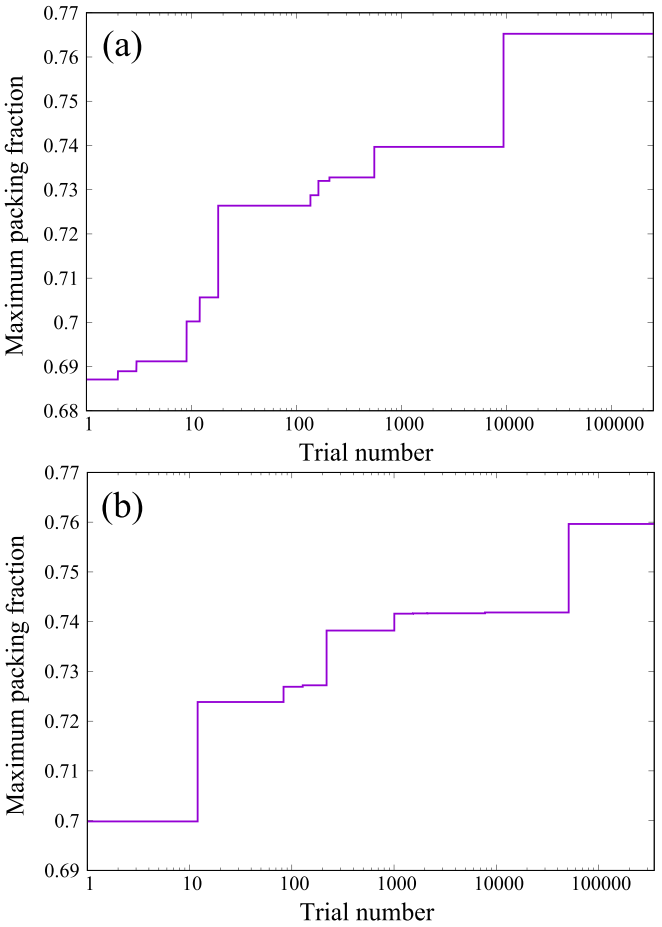

FIG. 6. The updating history of packing fractions during the exhaustive search. (a) The updating history for 14-5 system; the unit cell contains 14 small spheres and five large spheres. The radius ratio is $\alpha = 0.445$. (b) The updating history for 16-4 system; the unit cell contains 16 small spheres and four large spheres. The radius ratio is $\alpha = 0.455$.

packing fraction between 0.6850 and 0.6875 is 24 303 and the largest. On the other hand, the number of structures having the packing fraction between 0.7575 and 0.7600 is only eight. The result also indicates that our method can find the densest packings from the vast coordination space. Figure 6(b) shows the updating history of the packing fraction. The densest structure with the packing fraction of 0.759629 is generated at the 51 097th step.

IV. METHOD FOR PHASE DIAGRAM

In the previous sections, we have already discussed the details of our methods implemented in SAMLAI and the numerical aspects. In this section, we discuss how the phase diagram for DBSP is constructed with SAMLAI.

A. Exhaustive search conditions

To determine the densest phase separation at each composition ratio x and each radius ratio α, first the monophase DBSPs have to be identified at each (x, α).

To identify the monophase DBSPs at each (x, α), up to one million structures are generated with SAMLAI. We terminate the exhaustive search when the highest packing fraction is not updated 200 000 or 300 000 times, and regard the structure with the highest packing fraction as putative densest packing.

The radius ratio α is changed by a step of 0.02 in the range of $0.20 \leqslant \alpha \leqslant 0.64$ while the radius ratio is changed by a step of 0.005 in the radius range of $0.42 \leqslant \alpha \leqslant 0.50$. In total, the 35 radius ratios are investigated in the construction of the phase diagram.

The number of spheres in the unit cell is set between six and 24 while the number of spheres in the unit cell is set between 12 and 32 in the radius range of $0.42 \leqslant \alpha \leqslant 0.50$. Under the condition, all possible compositions are investigated with the constraint that the number of small spheres is equal to or larger than that of large spheres. In the former case, there are 138 compositions and in the latter case there are 220 compositions, respectively. In general, the number of possible compositions is $n^2/4$ if the maximum number of spheres is set to n, where n is an even number and the minimum number of spheres is set to two.

The optimization parameters are set to the default as discussed in Sec. III A.

B. Reoptimization

Almost all of the generated structures have an overlap of about 10^{-7} to 10^{-6}. Therefore, packing fractions may have an error on the sixth digit. In addition, the highest packing fraction may not be found due to a large number of local minima. Therefore, putative densest packings have to be reoptimized for determining the highest packing fractions with high accuracy. In some cases, tens of thousand steps for the reoptimization are necessary to find the highest packing fraction from the huge number of local minima. The reoptimization parameters are set to the defaults discussed in Sec. III D in most cases. In many cases, the reoptimization does not update the packing fractions while it updates the fourth digit and beyond of the packing fraction for cases that many local minima exist.

C. Phase separation

As Hopkins *et al.* have shown, for any given composition of m kinds of spheres, there is at least one phase separation with the densest packing fraction that consists of two or fewer structures when every structure is periodic [22]. We also proved it in a way that seems more intuitive to us. The proof is given in Appendix A. The densest phase separations are determined from all possible phase separations.

V. RESULT

In this section, we describe the discovered 12 putative DBSPs and the updated phase diagram. Next, we detail the geometry of DBSPs. Finally, we discuss geometric features of the monophase DBSPs.

A. Overview

We have discovered the 12 putative DBSPs and accordingly updated the phase diagram over the $x - \alpha$ plane, where

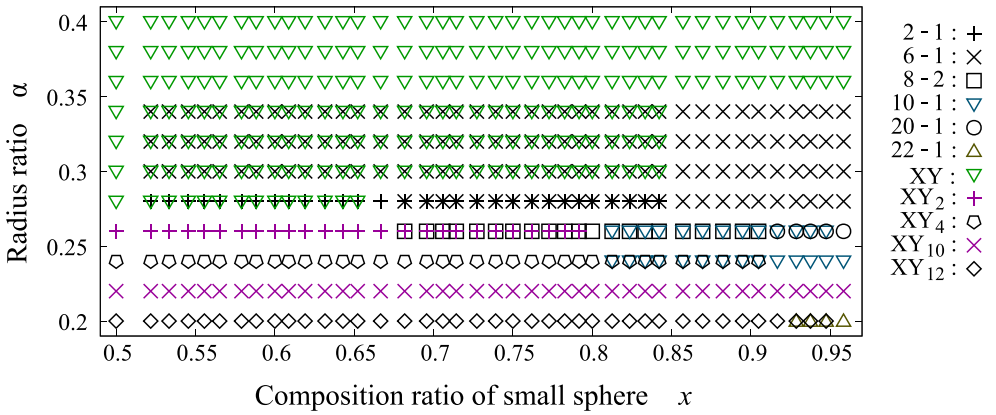

FIG. 7. The phase diagram in the radius ratio of $0.20 \leqslant \alpha \leqslant 0.40$. When the highest packing fraction is achieved by phase separation into a DBSP Φ and the fcc densest packing consisting of small or large spheres, only the symbol of the DBSP Φ is plotted. On the other hand, when the highest packing fraction is achieved by phase separation into two DBSPs, those two symbols are plotted together.

x is the relative concentration and α is the radius ratio of the small sphere relative to the large sphere. The phase diagram is shown in Fig. 7 for $0.20 \leqslant \alpha \leqslant 0.40$, Fig. 8 for $0.420 \leqslant \alpha \leqslant 0.500$, and Fig. 9 for $0.52 \leqslant \alpha \leqslant 0.64$, respectively. On the phase diagrams, 24 DBSPs are plotted. Some DBSPs are not plotted, e.g., the (12-1) structure and the (9-4) structure, because they appear in a very narrow region. For the case of 12 or fewer spheres in the unit cell, our phase diagram is consistent with the HST phase diagram [22] with a small correction.

The XY_n structures are defined as DBSPs in which large spheres X constitute the fcc densest structure and the small spheres Y penetrate into the tetrahedral and octahedral sites constituted by X. If the XY_n structures are excluded, there are 21 putative DBSPs. Most of those structures are named (m-n) structures. A (m-n) structure contains m small spheres and n large spheres. Their packing fractions are shown in Tables III–V.

For binary systems, the highest packing fraction is generally achieved by phase separation into two or fewer densest packings. When the highest packing fraction is achieved by phase separation into a DBSP Φ and the fcc densest packing consisting of small or large spheres, only the symbol of the DBSP Φ is plotted on the phase diagram. On the other hand, when the highest packing fraction is achieved by phase separation into two DBSPs, those two symbols are plotted together on the phase diagram. For example, in the area of $0.30 \leqslant \alpha \leqslant 0.34$ and $6/7 < x$, the highest packing fraction is achieved by the phase separation into the (6-1) structure and the fcc densest structure consisting of small spheres, and in the area of $0.30 \leqslant \alpha \leqslant 0.34$ and $1/2 < x < 6/7$ the highest packing fraction is achieved by the phase separation into the XY structure [22] and the (6-1) structure [22].

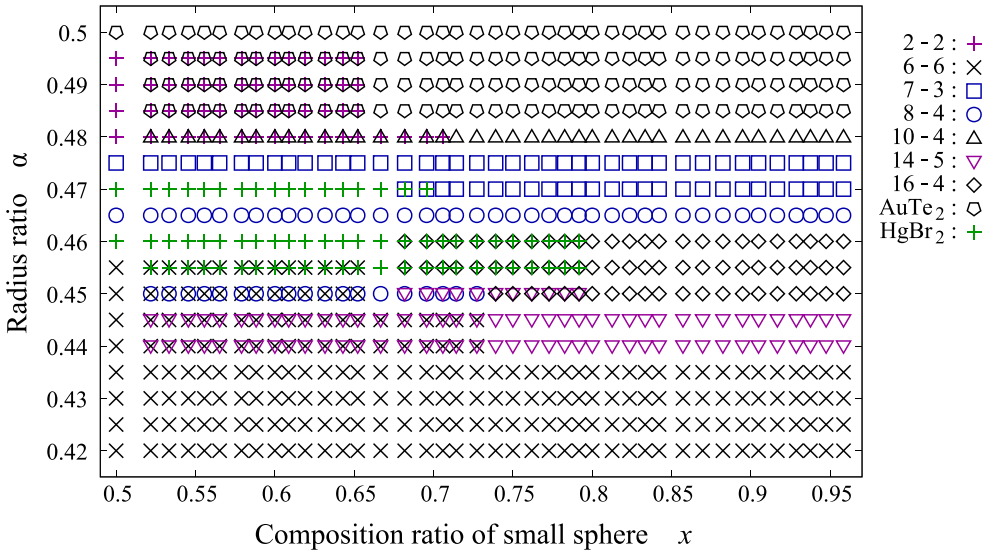

FIG. 8. The phase diagram in the radius ratio of $0.420 \leqslant \alpha \leqslant 0.500$. The rule in plotting symbols follows that explained in the caption of Fig. 7.

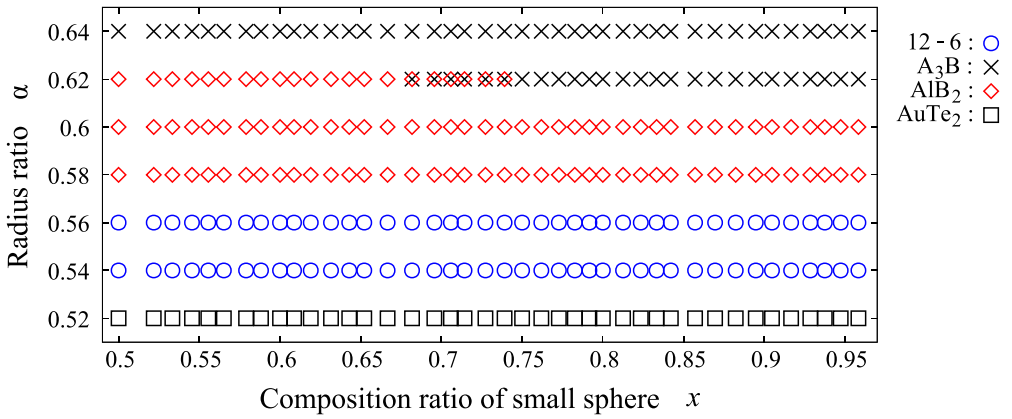

FIG. 9. The phase diagram in the radius ratio of $0.52 \leqslant \alpha \leqslant 0.64$. The rule in plotting symbols follows that explained in the caption of Fig. 7.

For $0.20 \leqslant \alpha \leqslant 0.40$, the exhaustive search is conducted for 11 radius ratios of 0.20, 0.22, 0.24, 0.26, 0.28, 0.30, 0.32, 0.34, 0.36, 0.38, and 0.40. The number of spheres in the unit cell is set between six and 24. By the exhaustive search, we have discovered six putative DBSPs: the XY_{12} structure, the (22-1) structure, the (12-1) structure, the (20-1) structure, the (8-2) structure, and the (2-1) structure. The XY_{12} structure and the (22-1) structure appear on the phase diagram at $\alpha = 0.20$ and 0.203. The (12-1) structure appears on the phase diagram at $\alpha = 0.203$; it can be understood as an extended XY_{12} structure. The (12-1) structure is not plotted on the phase diagram of Fig. 7, because it appears in a very narrow region. The (8-2) structure and the (20-1) structure appear on the phase diagram at $\alpha = 0.26$. The (8-2) structure is a distorted XY_4 structure. The (2-1) structure appears on the phase diagram at $\alpha = 0.28$; it is distorted XY_2 structure.

For $0.420 \leqslant \alpha \leqslant 0.500$, the exhaustive search is conducted for 17 radius ratios of 0.420, 0.425, 0.430, 0.435, 0.440, 0.445, 0.450, 0.455, 0.460, 0.465, 0.470, 0.475, 0.480, 0.485, 0.490, 0.495, and 0.500. The number of spheres in the unit cell is set between 12 and 32. By the exhaustive search, we have discovered five putative DBSPs: the (14-5) structure, the (16-4) structure, the (8-4) structure, the (10-4) structure, and the (9-4) structure. The (14-5) structure appears on the phase diagram at the three radius ratios of $\alpha = 0.440$, 0.445, and 0.450. The (16-4) structure appears on the phase diagram at the three radius ratios of $\alpha = 0.450$, 0.455, and 0.460. The (8-4) structure appears on the phase diagram at $\alpha = 0.450$ and 0.465 and it is isomorphic to the $HgBr_2$ structure. The (10-4) structure appears on the phase diagram at $\alpha = 0.480$ and 0.481; it is isomorphic to the (5-2) structure. The (9-4) structure appears on the phase diagram at the three radius ratios of $\alpha = 0.481$, 0.482, and 0.483. In addition, in contrast to the HST phase diagram, there is a phase separation into the (7-3) structure [22] and the $HgBr_2$ structure at $\alpha = 0.470$. Finally, the packing fractions of the $AuTe_2$ structure [13,22] are found to be consistent with those of the (4-2) structure [22]. Otherwise, the results are consistent with the HST phase diagram [22].

For $0.52 \leqslant \alpha \leqslant 0.64$, the exhaustive search is conducted for seven radius ratios of 0.52, 0.54, 0.56, 0.58, 0.60, 0.62, and 0.64. The number of spheres in the unit cell is set between six and 24. By the exhaustive search, we have discovered one putative DBSP: the (12-6) structure. It is isomorphic to the AlB_2 structure [13,22]. Otherwise, our phase diagram is consistent with the HST phase diagram [22].

In Secs. V B–V D, the densest packings in each radius range are detailed.

B. Densest packings for $0.20 \leqslant \alpha \leqslant 0.40$

For $0.20 \leqslant \alpha \leqslant 0.40$, the exhaustive search is conducted for 11 radius ratios of 0.20, 0.22, 0.24, 0.26, 0.28, 0.30, 0.32, 0.34, 0.36, 0.38, and 0.40. To confirm that the (12-1) structure appears on the phase diagram, the XY_{12} structure, the XY_{11} structure, and the (22-1) structure are reoptimized at $\alpha = 0.203$. The number of spheres in the unit cell is set between six and 24. As a result, we have discovered six putative DBSPs: the XY_{12} structure, the (22-1) structure, the (12-1) structure, the (20-1) structure, the (8-2) structure, and the (2-1) structure. Thereby, we update the phase diagram. For the case of 12 or fewer spheres in the unit cell, our phase diagram is consistent with that of the previous study [22] with a small correction. The putative DBSPs already discovered are the XY structure [22], the XY_2 structure [22], the XY_4 structure [22], the XY_8 structure [22], the XY_{10} structure [22], the XY_{11} structure [22], the (10-1) structure [22], the (11-1) structure [22], and the (6-1) structure [22]. The (10-1) structure and the (6-1) structure are shown in Fig. 10. In the radius ratio, large spheres tend to be surrounded by many small spheres as the (10-1) or (6-1) structures. On the phase diagram of Fig. 7, the XY_8 structure, the XY_{11} structure, and the (11-1) are not plotted, because they appear in the narrow region.

In this radius range, if the number of small spheres is small enough, all small spheres can penetrate into the tetrahedral and octahedral sites in the fcc densest structure constituted by large spheres. In that case, the packing fraction can be calculated as Eq. (17) even if the space is filled with phase separations consisting of more than one XY_n structure, because the volume of the voids in the fcc densest structure is constant. Hence, phase separation into several XY_n structures only complicates the phase diagram. Therefore, in our phase

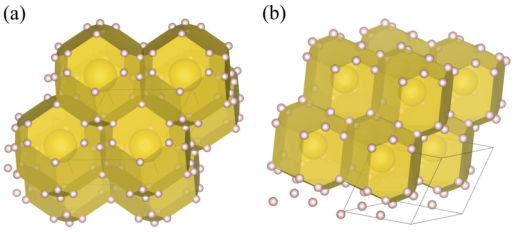

FIG. 10. Two examples of putative DBSPs already identified on the HST phase diagram in the radius ratio of $0.20 \leqslant \alpha \leqslant 0.40$ [22]. (a) The (10-1) structure; it is a distorted XY_{10} structure. (b) The (6-1) structure; it can be understood as a clathrate structure. It is an enlarged and distorted bcc structure consisting of the large spheres surrounded by small spheres.

diagram, the densest phase separation is represented by the XY_n structure which contains the largest number of small spheres. In other words, at each (α, x) only the XY_n structure which contains the largest number of small spheres is written on our phase diagram.

In this subsection, first we present a small difference from the HST phase diagram. Second, we present the discovered six putative DBSPs. Four of them have extended unit cells compared to the previous study [22].

1. Small difference from HST phase diagram

At $\alpha = 0.24$ and 0.26, the (10-1) structure appears on our phase diagram; the result is consitent with HST phase diagram. It is a distorted and expanded XY_{10} structure. The HST phase diagram also shows that in the area of $0.233 \leqslant \alpha \leqslant 0.245$ and $4/5 \leqslant x \leqslant 10/11$, the phase separation into the XY_{10} structure and the XY_4 structure is the densest, where large spheres of XY_{10} are arranged as in a Barlow packing with cubic symmetry but not in contact. We also found that at $\alpha = 0.239$, 0.240, and 0.242, the (10-1) structure becomes an expanded XY_{10} structure with cubic symmetry. However, at $\alpha = 0.236$, our result shows that the (10-1) structure is distorted without cubic symmetry. The result is inconsistent with that of Hopkins *et al.* [22]. Table III shows the packing fractions of the (10-1) structure at several radius ratios.

2. New putative densest sphere packings

In this section, we introduce the six putative DBSPs. Four of them have extended unit cells compared to the previous study [22].

The XY_{12} structure shown in Fig. 11(a) appears on the phase diagram at $\alpha = 0.20$ and the packing fraction is 0.811567. All of the small spheres penetrate into the tetrahedral and octahedral sites in the fcc densest structure constituted by large spheres. A tetrahedral site is occupied by one small sphere and an octahedral site is occupied by ten small spheres.

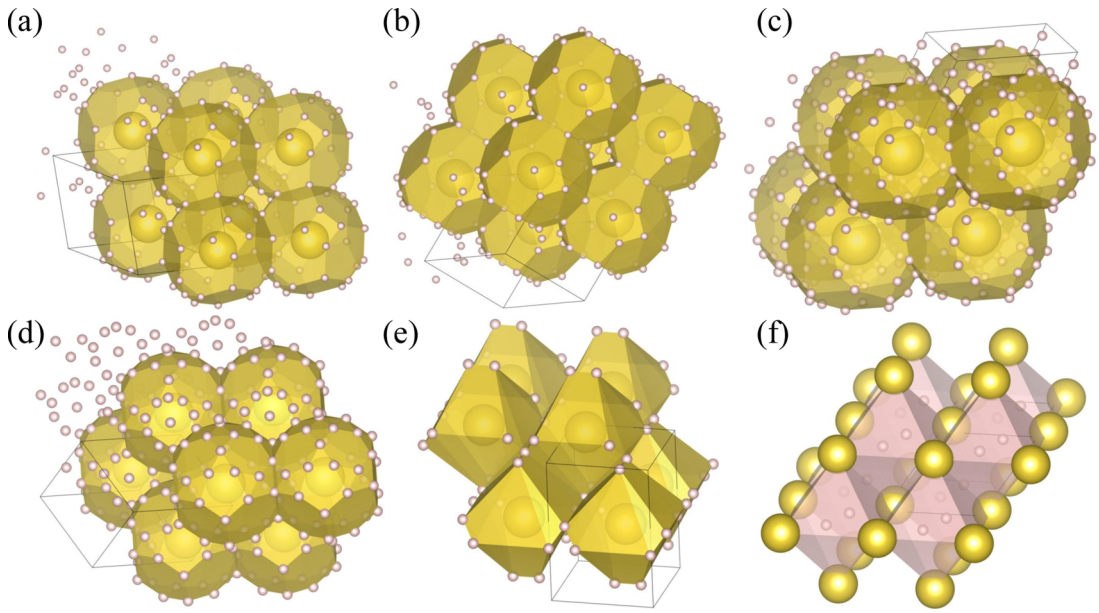

FIG. 11. Six DBSPs discovered in the radius ratio of $0.20 \leqslant \alpha \leqslant 0.40$. (a) The XY_{12} structure appears on the phase diagram at $\alpha = 0.20$ and the packing fraction is 0.811567. The unit cell contains 12 small spheres and one large sphere. (b) The (12-1) structure appears on the phase diagram at $\alpha = 0.203$ and the packing fraction is 0.811932. It can be understood as an extended XY_{12} structure. The unit cell contains 12 small spheres and one large sphere. It is not plotted on the phase diagram of Fig 7 because it appears in a very narrow region. (c) The (22-1) structure appears on the phase diagram at $\alpha = 0.20$ and 0.203. The packing fraction is 0.813313 and 0.809182, respectively. The unit cell contains 22 small spheres and one large sphere. (d) The (20-1) structure appears on the phase diagram at $\alpha = 0.26$ and the packing fraction is 0.785154. The unit cell contains 20 small spheres and one large sphere. (e) The (8-2) structure appears on the phase diagram at $\alpha = 0.26$, and the packing fraction is 0.788345. The unit cell contains eight small spheres and two large spheres. (f) The (2-1) structure appears on the phase diagram at $\alpha = 0.28$ and the packing fraction is 0.765223. The unit cell contains two small spheres and one large sphere.

The (12-1) structure shown in Fig. 11(b) appears on the phase diagram at $\alpha = 0.203$ and the packing fraction is 0.811932. The structure can be understood as an extended XY_{12} structure in one direction. An extended octahedral site is occupied by a rectangle which consists of eight small spheres with two small spheres inside the sides of the rectangle. It is not plotted on the phase diagram of Fig. 7 because it appears on the phase diagram in a very narrow region.

The (22-1) structure shown in Fig. 11(c) appears on the phase diagram at $\alpha = 0.20$ and 0.203. The packing fraction is 0.813313 and 0.809182, respectively. The structure can be understood as a distorted and expanded XY_{22} structure. We have confirmed that at $\alpha = 0.16$, the (22-1) structure becomes the XY_{22} structure, while we did not confirm that at $\alpha = 0.16$ how many small spheres at maximum can be placed in the voids of densest fcc structure constituted by large spheres.

The (20-1) structure shown in Fig. 11(d) appears on the phase diagram at $\alpha = 0.26$ and the packing fraction is 0.785154. The large spheres constitute a distorted face-centered orthohombic lattice. The structure can be understood as a clathrate structure. In this radius range, most of the structures, e.g., XY_{12}, (22-1), and (10-1), can be regarded as clathrate structure.

The (8-2) structure shown in Fig. 11(e) appears on the phase diagram at $\alpha = 0.26$ and the packing fraction is 0.788345. The structure can be understood as a distorted XY_4 structure without cubic symmetry. The HST phase diagram shows that the phase separation into the XY_4 structure and the XY_2 structure is the densest in the area of $0.258 \leqslant \alpha \leqslant 0.264$ and $2/3 \leqslant x \leqslant 4/5$, where large spheres of XY_4 are also arranged as in a Barlow packing with cubic symmetry but not in contact. We also find the expanded XY_4 structure, however, the packing fraction of the (8-2) structure is 0.000023 higher than that of the expanded XY_4 structure. Table III shows the packing fractions of the (8-2) structure at several radius ratios. At $\alpha = 0.261$ and 0.264, the (8-4) structure is also distorted.

The (2-1) structure shown in Fig. 11(f) appears on the phase diagram at $\alpha = 0.28$, while the HST phase diagram shows that the phase separation into the XY_2 structure and the XY structure is the densest in the area of $0.275 \leqslant \alpha \leqslant 0.278$ and $1/2 \leqslant x \leqslant 2/3$, where large spheres of XY_2 are arranged as in a Barlow packing with cubic symmetry but not in contact. The discovered (2-1) structure can be understood as a distorted XY_2 structure without cubic symmetry. The packing fraction of the structure is 0.765223. Table III shows the packing fractions of the (2-1) structure at several radius ratios. At $\alpha = 0.278$, the (2-1) structure does not have a cubic symmetry either.

C. Densest packings for $0.420 \leqslant \alpha \leqslant 0.500$

For $0.420 \leqslant \alpha \leqslant 0.500$, the exhaustive search is conducted for 17 radius ratios of 0.420, 0.425, 0.430, 0.435, 0.440, 0.445, 0.450, 0.455, 0.460, 0.465, 0.470, 0.475, 0.480, 0.485, 0.490, 0.495, and 0.500. To confirm that the (9-4) structure appears on the phase diagram, the (2-2) structure, the (10-4) structure, the $AuTe_2$ structure, and the (9-4) structure are reoptimized at $\alpha = 0.481$, 0.482, and 0.483. The number of spheres in the unit cell is set between 12 and 32. As a result,

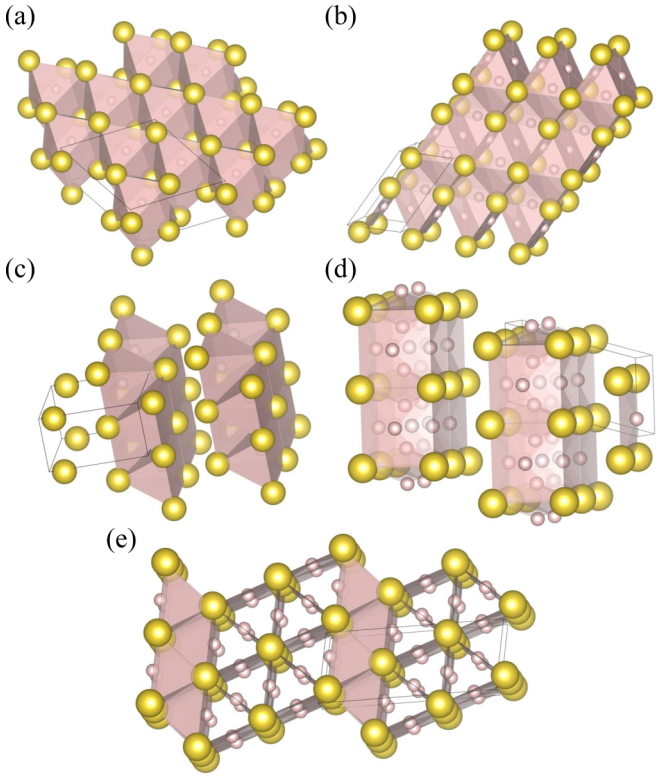

FIG. 12. The five putative DBSPs already identified on the HST phase diagram in the radius ratio of $0.420 \leqslant \alpha \leqslant 0.500$ [22]: (a) (6-6) structure, (b) $HgBr_2$ structure, (c) (2-2) structure, (d) (5-2) structure, and (e) (7-3) structure. The other two putative DBSP are shown in Fig. 13.

we have discovered five putative DBSPs: the (14-5) structure, the (16-4) structure, the (8-4) structure, the (10-4) structure, and the (9-4) structure. Thereby, we update the phase diagram. For the case of 12 or fewer spheres in the unit cell, our phase diagram is consistent with that of the previous study [22] with a small correction. The putative DBSPs already discovered are the (6-6) structure [22], the $HgBr_2$ structure [13,22], the (2-2) structure [22], the (5-2) structure [22], and the (7-3) structure [22] shown in Fig. 12, and the $AuTe_2$ structure [13,22] shown in Fig. 13.

In this subsection, first we present small modifications of the HST phase diagram for the case of 12 or fewer spheres in the unit cell. Second, we present the discovered five putative DBSPs. Four of them have extended unit cells compared to the previous study [22].

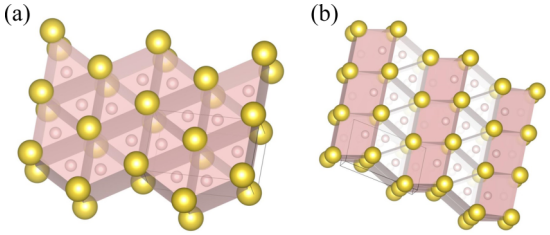

FIG. 13. (a) The $AuTe_2$ structure [13,22] and (b) the (4-2) structure [22]. In our calculations, it turns out that the packing fractions of the $AuTe_2$ structure is equal to that of the (4-2) structure.

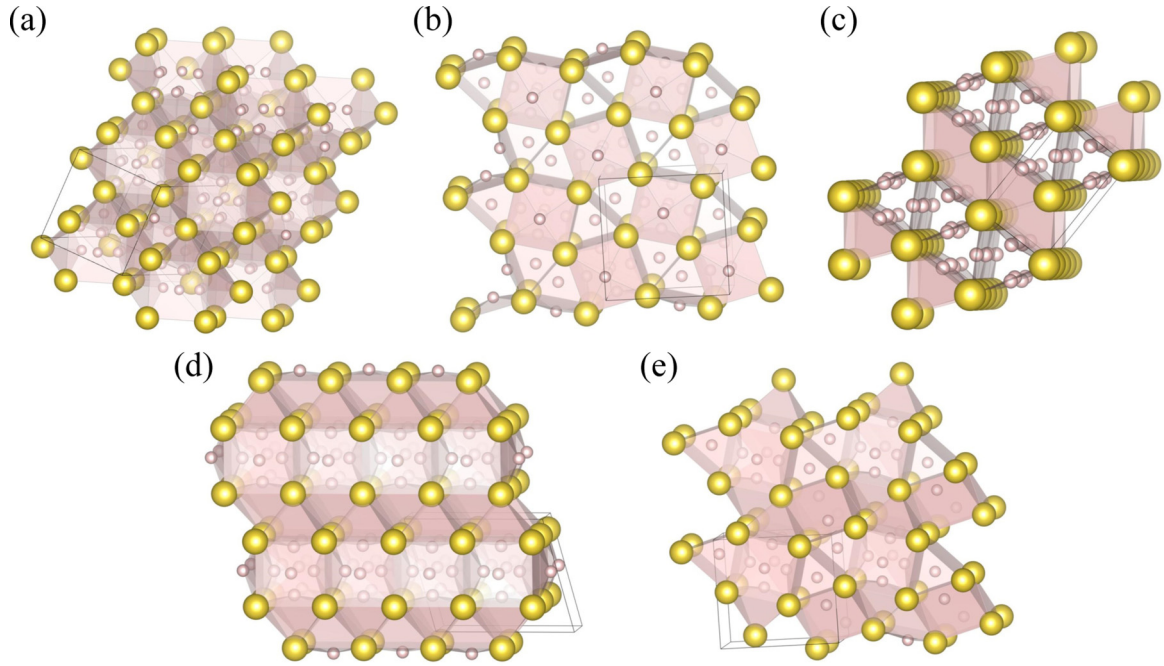

FIG. 14. Five putative DBSPs discovered in the radius ratio of $0.420 \leqslant \alpha \leqslant 0.500$. (a) The (14-5) structure appears on the phase diagram at the three radius ratios of $\alpha = 0.440$, 0.445, and 0.450. The packing fractions are 0.764247, 0.765259, and 0.759972, respectively. The unit cell contains 14 small spheres and five large spheres. (b) The (16-4) structure appears on the phase diagram at the three radius ratios of $\alpha = 0.450$, 0.455, and 0.460. The packing fractions are 0.760246, 0.759629, and 0.759276, respectively. The unit cell contains 16 small spheres and four large spheres. (c) The (8-4) structure appears on the phase diagram at $\alpha = 0.450$ and 0.465. The packing fraction is 0.758885 and 0.755714, respectively. The unit cell contains eight small spheres and four large spheres. The structure is isomorphic to the $HgBr_2$ structure. (d) The (10-4) structure appears on the phase diagram at two radius ratios of $\alpha = 0.480$ and 0.481. The packing fractions are 0.746216 and 0.746246, respectively. The unit cell contains ten small spheres and four large spheres. The structure is isomorphic to the (5-2) structure. (e) The (9-4) structure appears on the phase diagram at the three radial ratios of $\alpha = 0.481$, 0.482, and 0.483. The packing fractions are 0.746093, 0.746452, and 0.746510, respectively. The unit cell contains nine small spheres and four large spheres. The structure does not appear on the phase diagram of Fig. 8, because it appears in the narrow region.

1. Modifications of HST phase diagram

In our calculations, it turns out that the packing fractions of the $AuTe_2$ structure shown in Fig. 13(a) are equal to that of the (4-2) structure [22] shown in Fig. 13(b), at all of the radius ratios. The finding is inconsistent with the HST phase diagram. We provide a rational explanation below of why they should have the same packing fraction.

Both the $AuTe_2$ structure and the (4-2) structure are composed of triangular prisms with one small sphere. In the (4-2) structure, the orientation of the triangular prisms changes alternately. The triangular prism is distorted to increase the packing fraction. If the small radius is less than 0.5 where the large radius is 1, there are two kinds of triangular prisms. In the (4-2) structure, different triangular prisms are pointing in a different direction. An interface between those two triangular prisms is a square made of large spheres; the length of one side of the square is 2. One of the two small spheres in those two triangular prisms contacts the four large spheres; the small sphere is placed at the hollow in the center of the square. In that case, the triangular prism including the small sphere has two degrees of freedom in its direction, because the small sphere is in the middle of the square. In other words, there are two degrees of freedom of the arrangement on how to place the other two large spheres which constitute the triangular prism. These two degrees of freedom correspond to the $AuTe_2$ structure and the (4-2) structure. The other triangular prism has no freedom of the orientation if the small radius is less than 0.5 because the small sphere is not placed in the middle of the square. In conclusion, both the $AuTe_2$ structure and the (4-2) structure consist of the same triangular prisms, so they have the same packing fraction.

Finally, on our phase diagram, the phase separation into the $HgBr_2$ structure and the (7-3) structures appear at the radius ratio of $\alpha = 0.470$. The result is inconsistent with the HST phase diagram.

2. New putative densest sphere packings

In this section, we introduce the discovered five putative DBSPs. Four of them have extended unit cells compared to a previous study [22].

The (14-5) structure shown in Fig. 14(a) appears on the phase diagram at $\alpha = 0.440$, 0.445, and 0.450. The packing fractions are 0.764247, 0.765259, and 0.759972, respectively. The structure contains the 14-oligomer structures constituted by small spheres. The local structures are embedded in the gap among large spheres. A 14-oligomer structure consists of a cubic constituted by eight small spheres and six small spheres attached to each side of the cubic.

The (16-4) structure shown in Fig. 14(b) appears on the phase diagram at $\alpha = 0.450$, 0.455, and 0.460. The packing

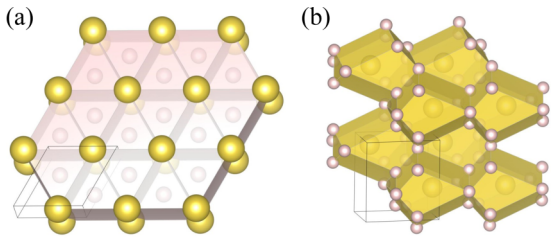

FIG. 15. Two of the three putative densest binary sphere packings already identified on the HST phase diagram in the radius ratio of $0.52 \leqslant \alpha \leqslant 0.64$ [22]. (a) AlB_2 structure. (b) A_3B structure.

fractions are 0.760246, 0.759629, and 0.759276, respectively. The structure consists of AlB_2-type local structure and cubic frameworks constituted by large spheres. A cubic framework is occupied by an octahedron consisting of small spheres.

The (8-4) structure shown in Fig. 14(c) appears on the phase diagram at $\alpha = 0.450$ and 0.465. The packing fractions are 0.758885 and 0.755714, respectively. Table IV shows the packing fractions of the structure at several radius ratios. The (8-4) structure is isomorphic to the $HgBr_2$ structure, but as shown in Table IV, the packing fractions of the (8-4) structure are higher than those of the $HgBr_2$ structure at some radius ratios: $\alpha = 0.431$, 0.434, 0.437, 0.440, 0.443, 0.445, 0.448, 0.463, and 0.465. At $\alpha = 0.450$, the packing fraction of the (8-4) structure is only 0.000002 higher than that of $HgBr_2$; however, in the radius range of $0.431 \leqslant \alpha \leqslant 0.450$, the (8-4) structure is denser than $HgBr_2$ structure. Therefore, it is likely true that the (8-4) structure is denser than the $HgBr_2$ structure at $\alpha = 0.450$.

The (10-4) structure shown in Fig. 14(d) appears on the phase diagram at $\alpha = 0.480$ and 0.481. The packing fractions are 0.746216 and 0.746246, respectively. The structure is isomorphic to the (5-2) structure but the packing fractions of (10-4) structure are higher than those of (5-2) structure.

Finally, the (9-4) structure shown in Fig. 14(e) appears on the phase diagram at the three radius ratios of $\alpha =$ 0.481, 0.482, and 0.483. The packing fractions are 0.746093, 0.746452, and 0.746510, respectively. The structure does not appear on the phase diagram of Fig. 8 because it appears in a very narrow region. The structure contains the (10-4)-type local structure.

D. Densest packings for $0.52 \leqslant \alpha \leqslant 0.64$

For $0.52 \leqslant \alpha \leqslant 0.64$, the exhaustive search is conducted for seven radius ratios of 0.52, 0.54, 0.56, 0.58, 0.60, 0.62, and 0.64. The number of spheres in the unit cell is set between six and 24. As a result, we have discovered one putative DBSP, named the (12-6) structure. The structure has an extended unit cell compared to the previous study [22]. Thereby, we update the phase diagram. For the case of 12 or fewer spheres in the unit cell, our phase diagram is completely consistent with that of the previous study [22]. The putative DBSPs already discovered are the $AuTe_2$ structure [13,22] shown in Fig. 13, the AlB_2 structure [13,22], and A_3B structure [14,22], shown in Fig. 15.

The (12-6) structure shown in Fig. 16 appears on the phase diagram at $\alpha = 0.54$ and 0.56. The packing fractions are 0.780466 and 0.779098, respectively. The structure can be understood as a distorted AlB_2 structure as well as the $AuTe_2$ structure. At these radius ratios, the $AuTe_2$ structure and the AlB_2 structure have the same packing fraction; the equivalence indicates that a large unit cell is necessary to realize an optimal distortion for higher packing fractions. At the three radius ratios of $\alpha = 0.58$, 0.60, and 0.62, the (12-6) structure and the AlB_2 structure have the same packing fraction; however, if the unit cell is expanded, a distorted AlB_2 structure might appear on the phase diagram. Further investigation will be in future work.

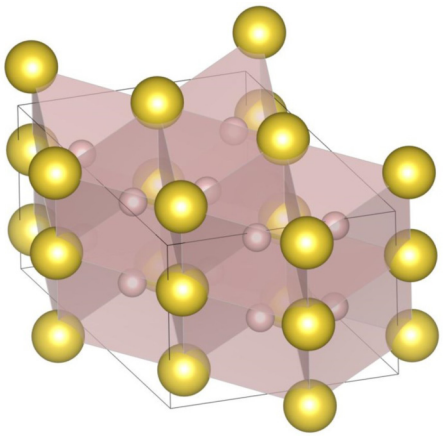

FIG. 16. The (12-6) structure appears on the phase diagram at $\alpha = 0.54$ and 0.56. The packing fractions are 0.780466 and 0.779098, respectively. The unit cell contains 12 small spheres and six large spheres. The structure is a distorted AlB_2 structure as well as the $AuTe_2$ structure.

E. Geometric features of densest packings

The putative DBSPs consist of local structures with high packing fraction. For example, the XY_n structure is clearly made up of a combination of local structures with high packing fractions: the tetrahedron and octahedron constituted by large spheres. The same is true for the distorted XY_n structure, such as (2-1), (8-2), (10-1), (11-1), and (22-1) structures. The same is also true for the (6-6) structure in which small spheres penetrate into the octahedral sites in the distorted hcp densest structure constituted by large spheres—similarly, the AlB_2 structure, the $AuTe_2$ structure, and the (12-6) structure consisting of the dense local structure in which a small sphere is embedded in the center of a triangular prism consisting of large spheres.

Some of the putative DBSPs are complex structures, especially for $0.42 \leqslant \alpha \leqslant 0.50$. Both the $HgBr_2$ structure and the (7-3) structure consist of equilateral triangular prisms and parallelepiped hexahedrons. The (10-4) structure consists of parallelepipedal hexahedrons and cubics constituted by large spheres with five small spheres. The (16-4) structure consists of an AlB_2-type local structure and cubic frameworks constituted by large spheres with an octahedron made of small spheres. In the (14-5) structure, 14-oligomer structures constituted by small spheres are embedded in the gap among the large spheres. As discussed below, these local structures also appear in monophase DBSPs that have lower packing

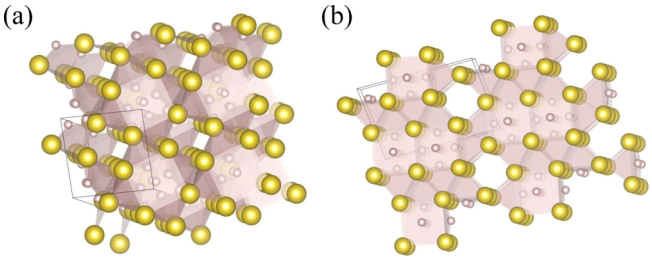

FIG. 17. (a) The (14-8) structure at $\alpha = 0.44$. It contains local structures of a 14-oligomer structure of small spheres embedded in the gap between the large spheres. Compared to the (14-5) structure, there are wasted gaps in it. (b) The (11-6) structure at $\alpha = 0.48$. It contains (10-4)-type local structure. Compared to the (10-4) structure, there are wasted gaps in it.

fractions than the densest phase separations. The appearance shows that those local structures are dense.

When space is filled with two kinds of spheres under periodic boundary conditions, the highest packing fraction is achieved by phase separation into two or fewer packing structures. However, in the below discussion, we prohibit a phase separation. Under the restriction, many monophase DBSPs are obtained.

Monophase DBSPs also consist of some of the dense local structures. The (14-8) structure is shown in Fig. 17(a). The structure is the densest at $(\alpha, x) = (0.44, 14/22)$. The unit cell contains 14 small spheres and eight large spheres. The structure contains 14-oligomer structures, which is the same local structure in the (14-5) structure. The (14-8) structure contains wasteful gaps compared to the (14-5) structure but the presence of the (14-5)-type local structure suggests that the local structure is dense. The (11-6) structure is shown in Fig. 17(b). The structure is the densest at $(\alpha, x) = (0.48, 11/17)$. The unit cell contains 11 small sphere and six large spheres. The structure contains the (10-4)-type local structure. The (11-6) structure contains a wasteful gap compared to the (10-4) structure but the presence of the (10-4)-type local structure indicates that the local structure is dense.

Some of the monophase densest sphere packings are long-period structures; those structures are phase separated into a few local structures in the unit cell. We discuss the two examples as such cases. First, the (9-5) structure is shown in Fig. 18. The structure is the densest at $(\alpha, x) = (0.46, 9/14)$. The unit cell contains nine small spheres and five large spheres. It consists of the $HgBr_2$-type triangular prism phase and the (6-6)-type stacking phase. The appearance of the $HgBr_2$-type local structure indicates that the local structure is dense at $\alpha = 0.46$. Second, the (16-6) structure is shown in Fig. 19. The structure is the densest at $(\alpha, x) = (0.56, 16/22)$. The unit cell contains 16 small spheres and six large spheres. It consists of the AlB_2-type triangular prism phase and the remainder of small spheres. The appearance of the AlB_2-type local structure indicates that the local structure is dense at $\alpha = 0.56$. The structural feature of the (16-6) structure indicates that the highest packing fraction at $(\alpha, x) = (0.56, 16/22)$ is achieved by phase separation into the AlB_2 structure and the fcc densest structure constituted by small spheres. In fact, our phase diagram shows that the highest packing fraction at $(\alpha, x) = (0.56, 16/22)$ is achieved by the phase separation into the (12-6) structure and fcc densest packing of small spheres.

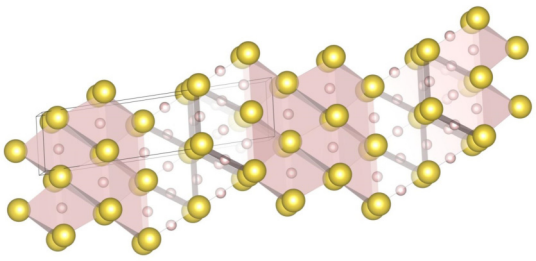

FIG. 18. The (9-5) structure at $\alpha = 0.46$. This structure consists of $HgBr_2$-type triangular prism phase and (6-6)-type stacking phase.

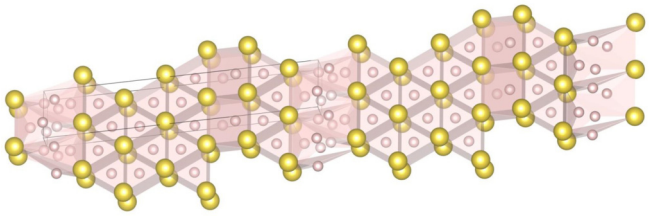

FIG. 19. The (16-6) structure at $\alpha = 0.56$. This structure consists of an AlB_2-type triangular prism phase and the remainder of a small spheres.

Those results show that all the monophase DBSPs are made of a few local structures with high packing fractions. The concept of dense local structures are very similar to the compact packing; the concept is defined for disk packings [37]. The compact packing corresponds to a structure in which all the circles are in contact with the perimeter and the gaps consist only of curvilinear triangles. It has been proved analytically that there are 164 ternary compact packings [37]. A local structure with a high packing fraction in the three-dimensional DBSPs may be regarded as an extended concept of compact packing for three dimensions.

VI. DISCUSSION

In this section, we detail the complexity of local minima, the effectiveness of our method, and the relationship between crystals and DBSPs.

A. Complexity of local minima

Sometimes the number of local minima becomes large. In this section, we discuss some representative examples, where the complexity of local minima can be understood.

First, we analytically compute the packing fraction of the $HgBr_2$ structure [13,22] shown in Fig. 12(b). Hereafter, the large radius is set to 1 and the small radius is set to r. The structure contains equilateral triangular prisms constituted by large spheres; the length of one side of the equilateral triangle is 2 and the height of the sides of the triangular prism is h. Small spheres are placed in the center of each side of the triangular prism and one of them is inserted inside until it touches the other two small spheres. We name the side K. In

that case, h can be calculated as

$$h = 2\sqrt{r^2 + 2r}. \tag{18}$$

The $HgBr_2$ structure also contains parallelepipedal hexahedrons. The bottom surface of the hexahedron is side K. One of the large spheres contacts the four large spheres which constitute the side K; here we assume that the large sphere does not overlap with the inserted small sphere. In that case, the height of parallelepiped hexahedron l can be calculated as

$$l = \sqrt{3 - \frac{h^2}{4}}. \tag{19}$$

The distance d between the large sphere and small sphere can be calculated as

$$d = \frac{\sqrt{3}}{2} - \sqrt{4r^2 - \frac{1}{4}} + l. \tag{20}$$

The $HgBr_2$ structure consists of two equilateral triangular prism and one parallelepiped hexahedron, so the packing fraction can be calculated as

$$\phi = \frac{2\pi(2 + 4r^3)}{3h\left(\sqrt{3} + \sqrt{3 - \frac{h^2}{4}}\right)}. \tag{21}$$

If we set the small sphere radius r as 0.46, d and ϕ are calculated as

$$d \simeq 1.4606503, \tag{22}$$

$$\phi \simeq 0.75900904. \tag{23}$$

On the other hand, the packing fraction calculated by SAMLAI is 0.759011. This small difference comes from the slight gap between small spheres; d is slightly larger than 1.46. The gap allows the two small spheres placed in the center of the sides of the equilateral triangular prism to penetrate slightly into the interior of the triangular prism; the distortion allows a slight increase in the packing fraction.

Second, the $HgBr_2$ structure and the (7-3) structure [22] shown in Fig. 12(e) are very similar. These two structures consist of equilateral triangular prisms and parallelepiped hexahedrons. The packing fraction is increased by small spheres penetrating slightly into the interior of triangular prisms. The parallelepiped hexahedron consisting of large spheres is necessary for periodic penetrating. In the region where the radius is getting larger, the (7-3) structure appears on the phase diagram instead of the $HgBr_2$ structure. This is because the (7-3) structure has twice as many triangular prisms as $HgBr_2$ structure; the connection of many triangular prisms is necessary for small spheres to penetrate into gaps in triangular prisms without making a wasted void between large spheres.

Third, the (10-1) structure [22] appears on the phase diagram at the two radius ratios of $\alpha = 0.240$ and 0.260. Table III shows the packing fractions of the (10-1) structure at several radius ratios. The (10-1) structure is an expanded or a distorted XY_{10} structure so small spheres can penetrate into the gap constituted by large spheres. The distortion pattern is varied according to the radius ratio. At most radius ratios, the (10-1) structure is distorted, but at $\alpha = 0.239$, 0.240, and 0.242, it becomes an enlarged XY_{10} structure whose symmetry is kept $Fm\bar{3}m$. We are surprised to find that the highly symmetric structure appears again at those radius ratios. This suggests that a delicate balance among the numerous distortion patterns determines which one has the highest packing fraction.

As we have discussed, the packing fraction is increased by distortions. Determining the maximum packing fraction becomes more difficult when the number of distortion patterns is larger. In addition, the unit cell is also related to the difficulty in determining the highest packing fraction.

Most of the densest packings are distorted; however, if the distortions are adjusted, some structures become highly symmetric and their unit cell could be reduced. For example, the unit cell of the $AuTe_2$ structure can be reduced to that of the AlB_2 structure [13,22] if the distortion of the $AuTe_2$ structure is adjusted. The unit cell of the AlB_2 structure and the $AuTe_2$ structure are shown in Figs. 20(a) and 20(b), respectively. In the $AuTe_2$ structure, the two large spheres in the unit cell are not in the same plane, so the highest packing fraction of the AlB_2 structure cannot be larger than that of the $AuTe_2$ structure. Furthermore, even if the unit cell of the AlB_2 structure is expanded, the highest packing fraction of the $AuTe_2$ structure is not always achievable. This is a representative example that a unit cell places a limit on the maximum packing fraction that can be reached. Hence, several isomorphic structures consisting of different unit cells need to be optimized to determine the maximum packing fraction. This is one of the main reasons why it is difficult to determine the maximum packing fraction.

TABLE II. Correspondence between crystals and densest sphere packings.

Densest sphere packing type	Crystal structure type	Space group	Material example
XY	NaCl	$Fm\bar{3}m$	NaCl, BaO, CeN
XY_2, (2-1)	KO_2	$I4/mmm$	KO_2, CaO_2, BaO_2
XY_{10}, (10-1)	–	$Fm\bar{3}m$	LaH_{10} [34]
(6-1)	–	$Im\bar{3}m$	YH_6 [32]
(6-6)	NiAs	$P6_3/mmc$	NiAs, FeSe, VP
(16-4)	UB_4	$P4/mbm$	UB_4, YB_4, LaB_4
(4-2)	$ThSi_2$	$I4_1/amd$	$ThSi_2$, $BeGe_2$, $SrGe_{2-\delta}$ [35]
(12-6), $AuTe_2$, AlB_2	AlB_2	$P6/mmm$	AlB_2, $ThSi_2$, $SrGa_2$
(2-2)	CaSi#AlTh	$Cmcm$	CaSi, AlTh, YSi
A_3B	Cu_3Ti	$Pmmn$	Cu_3Ti, Ni_3Nb, Au_3Sm

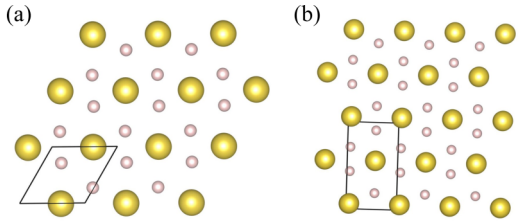

FIG. 20. A representative example that the unit cell can be reduced by adjusting the distortion. (a) The unit cell of the AlB_2 structure. (b) The unit cell of the $AuTe_2$ structure. The two large spheres in the unit cell are not in the same plane. The unit cell of the $AuTe_2$ is consistent with that of AlB_2 structure when the distortion is adjusted.

B. Effectiveness of iterative balance method

As discussed in the previous section, it is difficult to determine the maximum packing fraction. However, not only almost all the packing fractions calculated by our method are the same as those shown in the previous study [22] by more than three decimal points but also some of the packing fractions have successfully been updated. The results indicate that the iterative balance method can find the maximum packing fraction. In addition, the computational time for the structural optimization is very short, as discussed in Sec. III E. The effectiveness enables us to find the densest packing from the vast coordination space. Finally, as discussed in Sec. II C, the implementation is straightforward since it requires only simple calculations of forces and stress at each steepest descent step. The validity indicates that the iterative balance method might also be useful for the optimization of higher-dimensional sphere packings.

C. Effectiveness of piling-up method

As discussed in Sec. III F, our method can create diverse packing structures, so our method can discover a wide variety of monophase densest packings from the vast coordination space, as discussed in Sec. V E. The validity indicates that the piling-up method is an effective way to generate initial structures for predicting densest packings.

D. Public release of structural data and SAMLAI

Three-dimensional data of the DBSP and the SAMLAI package, in which our methods are implemented, are available online [38]. The distribution of the program package and the source codes follow the practice of the GNU General Public License version 3 (GPLv3).

E. Crystal structures and densest sphere packings

In some cases, atoms in crystals are approximated as spheres: In ion-bonded materials such as NaCl [4], atoms are often spherically symmetrical because atoms have closed-shell structures due to the charge transfer. In intermetallic compounds such as AgCu [5], atoms are also sometimes spherically symmetrical due to the bonds formed by electrons populating in s orbitals. In materials under high pressure, distances between atoms become so close that the directional orientation of the bond is weakened due to the strong repulsive force by Pauli's exclusion principle [6]. Therefore, we can assume that many crystals can be understood as densest sphere packings [4]. Then, we investigated the correspondence of DBSPs with the crystal structures with reference to the space groups. SPGLIB [39] is used for determining the space group of a densest sphere packing. The distortions of DBSPs are corrected by SPGLIB. As a result, we have succeeded in finding many crystals corresponding to DBSPs, e.g., LaH_{10} [34] and $SrGe_{2-\delta}$ [35] synthesized under high pressure, YH_6 [32] predicted theoretically under high pressure, and NaCl; their crystal structures correspond to the (4-2) structure [22], the XY_{10} structure [22], the (6-1) structure [22], and the XY structure [22], respectively. In addition, the crystal structure of UB_4 corresponds to the (16-4) structure. All of the correspondence we find is shown in Table II. This correspondence indicates that the densest sphere packings can be used effectively as structural prototypes for searching complex crystal structures, especially for high-pressure phases.

On the other hand, we could not find correspondence between crystals and the 15 DBSPs: XY_4, XY_8, XY_{11}, XY_{12}, (8-2), (11-1), (12-1), (20-1), (22-1), (14-5), (8-4), $HgBr_2$, (7-3), (10-4), and (9-4). However, we consider that these structures can be realized by crystals, e.g., the (20-1) structure and the (22-1) structure may be realized by hydrides. As discussed in Sec. V E, the DBSPs consist of a few local structures with high packing fractions. This is a different principle compared to crystals, but it is apparently true that the volume of a crystal structure is decreased as much as possible under high pressure, so many of the densest packings may correspond to crystals, especially for high-pressure phases.

VII. CONCLUSIONS

In the present research, we revisited the DBSPs under periodic boundary conditions. To efficiently explore the densest sphere packings, first we invented the *piling-up method* to generate initial structures in an unbiased way; second, we developed the *iterative balance method* to optimize the volume of a unit cell while keeping the overlap of hard spheres minimized. The piling-up method was developed based on the idea of stacking spheres randomly one by one on top of a randomly generated first layer. It enabled us to search the densest packings unbiasedly from the vast coordination space. The iterative balance method was developed based on the idea of repeating collision and repulsion among spheres under pressure while the maximum displacement in position vectors and lattice vectors was gradually decreased. The method not only generates a dense, periodic packing of nonoverlapping spheres but also predicts the maximum packing fraction with high accuracy. Those two methods are implemented in our open source program package SAMLAI.

With SAMLAI, we exhaustively searched the DBSPs by extending the unit cell compared to a previous study [22] and, as a result, we have discovered 12 putative DBSPs, named XY_{12}, (12-1), (22-1), (20-1), (8-2), (2-1), (14-5), (16-4), (8-4), (10-4), (9-4), and (12-6), shown in Figs. 11, 14, and 16. Accordingly, we have updated the phase diagram over the $x - \alpha$ plane, shown in Figs. 7–9. For the case of 12 or fewer spheres in the unit cell, our phase diagram is consistent with that

of the previous study [22] with a small correction. Through the exhaustive search, diverse monophase DBSPs have been discovered and accordingly we have found that high packing fractions are achieved by introducing a distortion and/or combining a few local dense structural units. Three-dimensional data of DBSPs and the SAMLAI package are available online [38].

If the XY_n structures are excluded, there are 21 putative DBSPs. Their packing fractions are shown in Tables . In some cases, it is difficult to determine the maximum packing fraction due to the large number of local minima corresponding to the large number of distortion patterns. However, comparing our results with those of the previous study [22], it is found that in most cases the packing fractions are consistent by more than three decimal points. Furthermore, some of the packing fractions are 0.001 larger. The results indicate that our method can identify the maximum packing fraction.

We examined the distribution and the update history of highest packing fraction during the exhaustive search. As a result, we have confirmed that diverse packing structures are created and our method can find the densest packings from diverse structures.

Furthermore, we have investigated the correspondence of the DBSPs with crystals based on the space group. The result shows that many structural units in real crystals, e.g., LaH_{10} [34] and $SrGe_{2-\delta}$ [35] synthesized under high pressure, can be understood as DBSPs. The correspondence implies that the densest sphere packings can be used effectively as structural prototypes for searching complex crystal structures, especially for high-pressure phases.

APPENDIX A: PHASE SEPARATION

As Hopkins *et al.* have shown, for any given composition of m kinds of spheres, there is at least one phase separation with the densest packing fraction that consists of less than or equal to m structures when every structure is periodic [22]. To present the paper in a self-contained manner, we provide a proof based on basic feasible solutions which might provide another perspective in understanding multinary densest sphere packings, while our proof is similar to that of Hopkins *et al.* [22] in a sense that both proofs are based on linear programming.

First, we fix the radius ratios of m kind of spheres. A set S is a collection of periodic structures including m kinds of fcc structures. The number of structures is s. The set S contains one of the densest structures at each composition ratio. The number of each sphere per unit cell of the structure k is given by $(n_{k1}, \cdots, n_{km})$. When a composition ratio $\boldsymbol{r} = (r_1, \cdots, r_m)$ is realized by phase separation into s kinds of structures, we have the following equations to be satisfied:

$$1 = \sum_{k=1}^{s} y_k, \tag{A1}$$

$$0 = \sum_{k=1}^{s} [r_j N_k - n_{kj}] y_k, \tag{A2}$$

$$0 \leqslant y_k, \tag{A3}$$

where $1 \leqslant j \leqslant m-1$, $N_k \equiv \sum_{l=1}^{m} n_{kl}$, and y_k is defined as

$$y_k \equiv \frac{b_k}{\sum_{i=1}^{s} b_i}, \tag{A4}$$

with b_k being the number of unit cell of the structure k. Equations (A1) and (A2) can be compactly written by introducing the matrix $A = (\boldsymbol{a}_1, \cdots, \boldsymbol{a}_s)$ as

$$\begin{pmatrix} 1 \\ 0 \\ \vdots \end{pmatrix} = A\boldsymbol{y}, \tag{A5}$$

where $\boldsymbol{a}_k$ is defined to be

$$\boldsymbol{a}_k^{\mathrm{T}} \equiv (1, N_k r_1 - n_{k1}, \cdots, N_k r_{m-1} - n_{k,m-1}). \tag{A6}$$

Under the constraints of Eqs. (A3) and (A5), The total packing fraction ϕ,

$$\phi = \frac{\sum_k y_k \, v_k \, \phi_k}{\sum_k y_k \, v_k}, \tag{A7}$$

is maximized, where v_k is the volume of unit cell of the structure k and ϕ_k is the packing fraction of the structure k.

The basic feasible solutions $\{\boldsymbol{z}_p\}$ of Eq. (A5) under Eq. (A3) can be obtained as follows: Let $\{b(1), \cdots, b(m)\}$ be subset from $\{1, \cdots, n\}$ and y_i is set to zero if $i \notin \{b(1), \cdots, b(m)\}$. Under the condition, $\boldsymbol{y}$ is determined uniquely if m-by-m submatrix $A_b = (\boldsymbol{a}_{b(1)}, \cdots, \boldsymbol{a}_{b(m)})$ is invertible. If all the components of the solution are not less than zero, the unique solution is one of the basic feasible solutions. Noting that the number of nonzero components of any basic feasible solution is less than or equal to m, it is found that the basic feasible solution corresponds to the phase separation consisting of less than or equal to m different structures.

All feasible solutions $\boldsymbol{y} = (y_1, \cdots, y_s)$ can be expressed as a convex combination of basic feasible solutions,

$$\boldsymbol{y} = \sum_p w_p \boldsymbol{z}_p, \tag{A8}$$

because $\boldsymbol{y}$ is bounded [40,41]. Therefore, Eq. (A7) can be rewritten as

$$\phi = \frac{\boldsymbol{y} \cdot \boldsymbol{S}}{\boldsymbol{y} \cdot \boldsymbol{V}} = \frac{\sum_p w_p \boldsymbol{z}_p \cdot \boldsymbol{S}}{\sum_k w_p \boldsymbol{z}_p \cdot \boldsymbol{V}}, \tag{A9}$$

where $\boldsymbol{V} = (v_1, \cdots, v_n)$ and $\boldsymbol{S} = (v_1\phi_1, \cdots, v_n\phi_n)$. Introducing $\tilde{v}_p$ as

$$\tilde{v}_p \equiv \boldsymbol{z}_p \cdot \boldsymbol{V} = \sum_l y_{pl} \, v_l, \tag{A10}$$

and $\tilde{\phi}_p$ as

$$\tilde{\phi}_p \equiv \frac{\boldsymbol{z}_p \cdot \boldsymbol{S}}{\boldsymbol{z}_p \cdot \boldsymbol{V}} = \frac{\sum_l y_{pl} \, v_l \, \phi_l}{\sum_l y_{pl} \, v_l}, \tag{A11}$$

where $\boldsymbol{z}_p = (y_{p1}, \cdots, y_{pn})$, we can rewrite Eq. (A9) as

$$\phi = \frac{\sum_p w_p \tilde{v}_p \tilde{\phi}_p}{\sum_p w_p \tilde{v}_p}. \tag{A12}$$

TABLE III. The packing fractions of the DBSPs in the radius ratio of $0.200 \leqslant \alpha \leqslant 0.352$. The XY_n-type structures are excluded. Compared to the HST phase diagram [22], the larger packing fractions are shown in bold and the smaller ones are shown in italics.

α	(22-1)	(12-1)	(11-1)	(10-1)	(20-1)	(6-1)	(8-2)	(2-1)
0.200	0.813313							
0.203	0.809182	0.811932						
0.206	0.805783	0.807009						
0.209	0.801278	0.802364						
0.212	0.797876	0.799775						
0.214	0.796231	0.799418						
0.217	0.794616	0.796801	0.822630					
0.220	0.792056	0.794140	0.817957					
0.223	0.790229	0.791817	0.814383					
0.225			0.811122	*0.824311*				
0.228				0.821822				
0.230				0.820323				
0.233				0.817962				
0.236				0.815926				
0.239				0.812289				
0.242				0.807668	0.782166			
0.245				*0.803451*	0.781966			
0.247				**0.800974**	0.782001			
0.250				**0.797510**	0.782303			
0.253				0.794335	0.782890			
0.256				0.791435	0.783738			
0.258				**0.789649**	0.784441			
0.261				0.787181	0.785285		0.786449	
0.264				0.784959	0.783329	*0.780418*	0.780930	
0.267				0.782973	0.778084	0.781892	0.775655	
0.270				0.781213	0.773025	0.783601	0.770617	
0.273					0.768679	**0.785533**	0.768293	
0.275					0.766132	0.786941	0.767796	
0.278					0.762136	0.789225	0.767489	0.767544
0.281						0.791710		0.764182
0.284						0.794388		0.761459
0.287						0.797252		0.759235
0.289						*0.799263*		0.757982
0.292						0.800869		0.756394
0.295						0.799598		0.755110
0.298						0.798549		0.754086
0.301						0.797714		
0.304						0.797085		
0.307						0.796654		
0.309						0.796068		
0.312						0.794900		
0.315						0.793889		
0.318						0.793034		
0.321						0.791582		
0.324						0.788239		
0.326						0.786121		
0.329						0.783107		
0.332						0.780285		
0.335						0.777650		
0.338						0.775199		
0.341						0.772928		
0.343						**0.771512**		
0.346						**0.769533**		
0.349						0.767724		
0.352						0.766084		

TABLE IV. The packing fractions of the DBSP in the radius ratio of $0.414 \leqslant \alpha \leqslant 0.500$. Compared to the HST phase diagram [22], the larger packing fractions are shown in bold and the smaller ones are shown in italics while the packing fractions of the (7-3) structure are shown normally.

α	(16-4)	(14-5)	(10-4)	(9-4)	(8-4)	$HgBr_2$	(7-3)	$AuTe_2$	(6-6)	(2-2)
0.414									0.793023	
0.417									**0.789534**	
0.420									0.785872	
0.423									*0.782347*	
0.426									0.778968	
0.428									**0.776794**	
0.431		0.755399			0.760930	0.760315			**0.773646**	
0.434		0.758308			0.760710	0.759992			0.770629	
0.437		0.761257			0.760455	0.759726			0.767739	
0.440		0.764247			0.760144	0.759518			0.764971	
0.443	0.757311	0.767278			0.759747	0.759365			*0.762320*	
0.445	0.759701	0.765259			0.759348	0.759294			**0.760616**	
0.448	0.760568	0.762049			0.759041	0.759035			0.758151	
0.451	0.760101	0.758952			0.758830	0.758830			0.755793	
0.454	0.759731	0.755967			0.758762	0.758762			0.753537	
0.457	0.759456	0.753092			0.758825	0.758825			0.751380	
0.460	0.759276	0.750298			0.759011	0.759011			0.749319	
0.463	0.754469				0.757833	0.757814	0.750988			
0.465	0.750732				0.755714	0.755701	0.751180			
0.468	0.745076				0.752668	0.752668	0.751510			
0.471			0.746408	0.743894	0.749796	0.749796	0.750015			0.741836
0.474			0.746249	0.744177	0.747076	0.747076	0.747831	0.740802		0.742356
0.477			0.746185	0.744854	0.744506	0.744506	0.745776	0.742471		0.742966
0.480			0.746216	0.745757			0.743866	0.744233		0.743661
0.481			0.746246	0.746093			0.743257	0.744840		0.743911
0.482			0.746287	0.746452			0.742661	0.745457		0.744170
0.483			0.746337	0.746510			0.742080	0.746084		0.744437
0.485			0.746468	0.746117			0.740956	*0.747366*		0.744997
0.488			0.746727	0.745626				*0.749358*		0.745898
0.491								0.751431		0.746869
0.494								0.753583		0.747907
0.497								0.755810		0.749010
0.500								0.758114		0.750174

If we choose $\tilde{\phi}_1$ as the highest among $\{\tilde{\phi}_k\}$, the packing fraction ϕ can be rewritten as

$$\phi = \tilde{\phi}_1 - \frac{\sum_p w_p \tilde{v}_p (\tilde{\phi}_1 - \tilde{\phi}_p)}{\sum_p w_p \tilde{v}_p}. \tag{A13}$$

Noting that $\tilde{\phi}_p$ is the packing fraction of basic phase separation z_p and all the basic feasible solutions possess the same composition ratio of $\boldsymbol{r}$, it turns out that the highest packing fraction $\tilde{\phi}_1$ can be achieved by selecting the basic feasible solution corresponding to $\tilde{\phi}_1$. Every basic feasible solution consists of less than or equal to m structures, and therefore, we have proved that for any given composition of m kinds of spheres, the highest packing fraction can be achieved by the densest phase separation that consists of less than or equal to m structures. Note that the total densest packing fraction can also be achieved by phase separation consisting of more than m kind of structures if some basic feasible solutions have the same highest packing fraction, as discussed in Ref. [22].

APPENDIX B: PACKING FRACTIONS

If the XY_n structures are excluded, there are 21 putative DBSPs. Their packing fractions are shown in Tables III–V. The tables include all the radius ratio shown in Table I in Ref. [22]. Comparing our results with those of the previous study [22], it is found that in most cases the packing fractions are consistent by more than three decimal points.

However, some of the packing fractions are 0.001 larger or smaller. In Tables III–V, they are shown in bold or italics, respectively. The difference between ours and those in Ref. [22] might be due to rounding. The radius ratios shown in Table I in Ref. [22] are rounded to the third decimal place while the radius ratios shown in our paper is not rounded. The difference means that we may use different radius ratios compared to the previous study [22].

The packing fractions shown in the tables are determined by reoptimization. When the number of local minima is small, almost all the reoptimized structures converge to the densest packing. On the other hand, when the number of local minima is large, we obtain many packing fractions corresponding to

TABLE V. The packing fractions of the DBSPs in the radius ratio of $0.537 \leqslant \alpha \leqslant 0.64$. Compared to the HST phase diagram [22], the larger packing fractions are shown in bold and the smaller ones are shown in italics.

α	$AuTe_2$	AlB_2	(12-6)	A_3B
0.537	0.780598	0.780598	0.780743	
0.540	0.780217	0.780217	0.780466	
0.543	0.779883	0.779883	0.780262	
0.546	0.779595	0.779595	0.780130	
0.549	0.779352	0.779352	0.780067	
0.552		0.779154	0.779719	
0.554		0.779046	0.779522	
0.557		0.778922	0.779280	
0.560		0.778841	0.779098	
0.563		0.778804	0.778977	
0.566		0.778808	0.778916	
0.569		0.778856	0.778913	
0.572		0.778944	0.778968	
0.574		0.779027	0.779036	
0.577		0.779184	0.779184	
0.580		0.776382	0.776382	
...				
0.612		0.748108		0.743387
0.614		0.746679		0.743268
0.617		0.744608		0.743174
0.620		0.742622		0.743180
0.623		0.740720		0.743285
...				
0.640				0.745690

diverse distortion patterns in the reoptimization process. This is because many structures are trapped at local minima. In that case, the large number of reoptimizations is necessary to determine the highest packing fraction. In some cases, tens of thousand of reoptimizations are necessary.

At the radius ratio $\alpha = 0.480$, the packing fraction of the (7-3) structure shown in Table I in Ref. [22] is in contradiction with the HST phase diagram [22]. The HST phase diagram shows that the packing fraction of the (7-3) structure is the same as that of the phase separation into the (4-2) structure and the (5-2) structure. However, Table I in Ref. [22] shows that the packing fraction of the (7-3) structure is higher than that of the (4-2) structure and the (5-2) structure. If the space is filled with two structures, the packing fraction is not higher than the denser packing fraction of the two. Our calculation shows that the packing fractions of the (7-3) structure are less than those of the (4-2) structure and the (5-2) structure. Of course, we may be failing to discover the highest packing fractions but we guess that they are less than those shown in Table I in Ref. [22] at some radius ratios. Therefore, the packing fractions of the (7-3) structure are shown normally in Table IV.

APPENDIX C: DERIVATIVES OF THE ENTHALPY

In our method, lattice vectors and the position vectors are simultaneously optimized by using the steepest descent method. To apply the steepest descent method, we need to calculate the derivatives of the enthalpy. In this section, we explain how to derive the derivatives analytically.

First, we define matrix A as

$$A \equiv \begin{pmatrix} a_{11} & a_{21} & a_{31} \\ a_{12} & a_{22} & a_{32} \\ a_{13} & a_{23} & a_{33} \end{pmatrix}, \tag{C1}$$

where $\boldsymbol{a}_1$, $\boldsymbol{a}_2$, and $\boldsymbol{a}_3$ are the lattice vectors. The x, y, and z components of vector $\boldsymbol{a}_i$ is written as a_{i1}, a_{i2}, and a_{i3}, respectively. Matrix C is defined as

$$C \equiv \begin{pmatrix} \boldsymbol{a}_1 \cdot \boldsymbol{a}_1 & \boldsymbol{a}_2 \cdot \boldsymbol{a}_1 & \boldsymbol{a}_3 \cdot \boldsymbol{a}_1 \\ \boldsymbol{a}_1 \cdot \boldsymbol{a}_2 & \boldsymbol{a}_2 \cdot \boldsymbol{a}_2 & \boldsymbol{a}_3 \cdot \boldsymbol{a}_2 \\ \boldsymbol{a}_1 \cdot \boldsymbol{a}_3 & \boldsymbol{a}_2 \cdot \boldsymbol{a}_3 & \boldsymbol{a}_3 \cdot \boldsymbol{a}_3 \end{pmatrix}. \tag{C2}$$

Hereafter, the position of sphere i is represented by $\boldsymbol{r}_i$ and the fractional coordinates are represented by $\boldsymbol{q}_i = (q_{i1}, q_{i2}, q_{i3})$. The relative fractional coordinate $\boldsymbol{q}_{ij}^{(\boldsymbol{Q})}$ is defined as

$$\boldsymbol{q}_{ij}^{(\boldsymbol{Q})} \equiv \boldsymbol{q}_j + \boldsymbol{Q} - \boldsymbol{q}_i, \tag{C3}$$

where $\boldsymbol{Q}$ is defined as integer vector. The relative vector $\boldsymbol{r}_{ij}^{(\boldsymbol{Q})}$ is defined as

$$\boldsymbol{r}_{ij}^{(\boldsymbol{Q})} \equiv \boldsymbol{r}_j + \boldsymbol{T} - \boldsymbol{r}_i = A\boldsymbol{q}_{ij}^{(\boldsymbol{Q})}, \tag{C4}$$

where $\boldsymbol{T}$ are translational vectors that satisfy the equation as $\boldsymbol{T} = A\boldsymbol{Q}$. Taking the absolute value of Eq. (C4) leads to

$$r_{ij}^{(\boldsymbol{Q})} \equiv |\boldsymbol{r}_j + \boldsymbol{T} - \boldsymbol{r}_i| = \sqrt{{}^t\boldsymbol{q}_{ij}^{(\boldsymbol{Q})} C \boldsymbol{q}_{ij}^{(\boldsymbol{Q})}}. \tag{C5}$$

Finally, we define $z_{ij}^{(\boldsymbol{Q})}$ as

$$z_{ij}^{(\boldsymbol{Q})} \equiv r_{ij}^{(\boldsymbol{Q})} - (c_i + c_j), \tag{C6}$$

where c_i is defined as the radius of the sphere i.

The potential working between spheres is defined as Eq. (10) and the total energy per unit cell E is given by Eq. (9). The enthalpy per unit cell H is given by

$$H = \frac{1}{2}\sum_{\boldsymbol{Q}}\sum_{i=1}^{N}\sum_{j=1}^{N} U\left(z_{ij}^{(\boldsymbol{Q})}\right) + PV. \tag{C7}$$

The volume V can be calculated as

$$V = |\mathrm{det}A| = |\boldsymbol{a}_1 \cdot (\boldsymbol{a}_2 \times \boldsymbol{a}_3)|. \tag{C8}$$

If we take the lattice vectors to a right-handed system, V can be calculated as $V = \mathrm{det}A$. We set the initial lattice vector to the right-handed system.

The derivative of the enthalpy with respect to q_{ik} can be calculated as

$$\frac{\partial E}{\partial q_{ik}} = \sum_{\boldsymbol{Q}}\sum_{j=1}^{N} \frac{\partial r_{ij}^{(\boldsymbol{Q})}}{\partial q_{ik}} \cdot f\left(z_{ij}^{(\boldsymbol{Q})}\right), \tag{C9}$$

where $f(z_{ij}^{(\boldsymbol{Q})})$ is defined as

$$f\left(z_{ij}^{(\boldsymbol{Q})}\right) \equiv \frac{\partial U\left(z_{ij}^{(\boldsymbol{Q})}\right)}{\partial z_{ij}^{(\boldsymbol{Q})}} = \begin{cases} -1 & z_{ij}^{(\boldsymbol{T})} \leqslant 0 \\ 0 & 0 < z_{ij}^{(\boldsymbol{T})} \end{cases}. \tag{C10}$$

The derivative of $r_{ij}^{(\boldsymbol{Q})}$ with respect to q_{ik} can be calculated as

$$\frac{\partial r_{ij}^{(\boldsymbol{Q})}}{\partial q_{ik}} = -\frac{1}{r_{ij}^{(\boldsymbol{Q})}}\sum_{t=1}^{3} c_{kt}\, q_{ij,t}^{(\boldsymbol{Q})}. \tag{C11}$$

The derivative of the enthalpy with respect to a_{mn} can be calculated as

$$\frac{\partial H}{\partial a_{mn}} = \frac{\partial E}{\partial a_{mn}} + P\frac{\partial V}{\partial a_{mn}}. \tag{C12}$$

The first term of Eq. (C12) can be calculated as

$$\frac{\partial E}{\partial a_{mn}} = \frac{1}{2}\sum_{\boldsymbol{Q}}\sum_{i=1}^{N}\sum_{j=1}^{N} \frac{\partial r_{ij}^{(\boldsymbol{Q})}}{\partial a_{mn}} \cdot f\left(z_{ij}^{(\boldsymbol{Q})}\right), \tag{C13}$$

where the derivative of $r_{ij}^{(\boldsymbol{Q})}$ with respect to a_{mn} can be calculated as

$$\frac{\partial r_{ij}^{(\boldsymbol{Q})}}{\partial a_{mn}} = \frac{1}{r_{ij}^{(\boldsymbol{Q})}}\sum_{s=1}^{3} a_{sn}\, q_{ij,s}^{(\boldsymbol{Q})}\, q_{ij,m}^{(\boldsymbol{Q})}. \tag{C14}$$

The second term of Eq. (C12) can be calculated as

$$P\frac{\partial V}{\partial a_{mn}} = \frac{1}{2}P\sum_{i,j}\sum_{k,l} \epsilon_{mij}\,\epsilon_{nkl}\,a_{ik}\,a_{jl}, \tag{C15}$$

where ϵ_{ijk} is the Levi-Civita symbol.

If the neighboring list of each sphere is reused a few hundred times, the lattice vectors accidentally may change from a right-handed system to a left-handed system due to the spheres slipping through each other. The slipping is a fatal accident for structural optimization. The change causes a negative value of $\Omega = \mathrm{det}A$, so we can confirm that a structure is normally optimized by checking the sign of V.

[1] R. A. LaCour, C. S. Adorf, J. Dshemuchadse, and S. C. Glotzer, ACS Nano **13**, 13829 (2019).
[2] M. A. Boles, M. Engel, and D. V. Talapin, Chem. Rev. **116**, 11220 (2016).
[3] M. Leocmach, J. Russo, and H. Tanaka, J. Chem. Phys. **138**, 12A536 (2013).
[4] P. Villars, in *Intermetallic Compounds*, edited by J. H. Westbrook and R. L. Fleischer (Wiley, New York, 2000), Vol. 1, Chap. 1, pp. 1–49.
[5] P. R. Subramanian and J. H. Perepezko, J. Phase Equilib. **14**, 62 (1993).
[6] M. Rahm, R. Cammi, N. W. Ashcroft, and R. Hoffmann, J. Am. Chem. Soc. **141**, 10253 (2019).
[7] A. Umayahara and M. Nespolo, Z. Kristallogr. - Cryst. Mater. **233**, 179 (2018).
[8] T. C. Hales, Ann. Math. **162**, 1065 (2005).
[9] H. J. H. Brouwers, Phys. Rev. E **76**, 041304 (2007).
[10] H. J. H. Brouwers, Phys. Rev. E **78**, 011303 (2008).
[11] H. J. H. Brouwers, Phys. Rev. E **87**, 032202 (2013).
[12] J. K. Kummerfeld, T. S. Hudson, and P. Harrowell, J. Phys. Chem. B **112**, 10773 (2008).
[13] L. Filion and M. Dijkstra, Phys. Rev. E **79**, 046714 (2009).
[14] P. I. O'Toole and T. S. Hudson, J. Phys. Chem. C **115**, 19037 (2011).
[15] T. S. Hudson, J. Phys. Chem. C **114**, 14013 (2010).
[16] T. S. Hudson and P. Harrowell, J. Phys.: Condens. Matter **23**, 194103 (2011).
[17] D. Wang, X. An, D. Gou, H. Zhao, L. Wang, and F. Huang, AIP Adv. **8**, 105203 (2018).
[18] D. De Laat, F. M. de Oliveira Filho, and F. Vallentin, in *Forum of Mathematics, Sigma* (Cambridge University Press, 2014), Vol. 1.
[19] S. Torquato, *Random Heterogeneous Materials: Microstructure and Macroscopic Properties*, Interdisciplinary Applied Mathematics (Springer, New York, 2013).
[20] S. Torquato and Y. Jiao, Phys. Rev. E **82**, 061302 (2010).
[21] A. B. Hopkins, Y. Jiao, F. H. Stillinger, and S. Torquato, Phys. Rev. Lett. **107**, 125501 (2011).
[22] A. B. Hopkins, F. H. Stillinger, and S. Torquato, Phys. Rev. E **85**, 021130 (2012).
[23] C. W. Glass, A. R. Oganov, and N. Hansen, Comput. Phys. Commun. **175**, 713 (2006).
[24] A. R. Oganov and C. W. Glass, J. Chem. Phys. **124**, 244704 (2006).

[25] A. R. Oganov and C. W. Glass, J. Phys.: Condens. Matter **20**, 064210 (2008).
[26] A. O. Lyakhov, A. R. Oganov, and M. Valle, Comput. Phys. Commun. **181**, 1623 (2010).
[27] A. O. Lyakhov, A. R. Oganov, H. T. Stokes, and Q. Zhu, Comput. Phys. Commun. **184**, 1172 (2013).
[28] Y. Wang, J. Lv, L. Zhu, and Y. Ma, Phys. Rev. B **82**, 094116 (2010).
[29] Y. Wang, J. Lv, L. Zhu, and Y. Ma, Comput. Phys. Commun. **183**, 2063 (2012).
[30] Y. Wang, J. Lv, L. Zhu, S. Lu, K. Yin, Q. Li, H. Wang, L. Zhang, and Y. Ma, J. Phys.: Condens. Matter **27**, 203203 (2015).
[31] H. Wang, Y. Wang, J. Lv, Q. Li, L. Zhang, and Y. Ma, Comput. Mater. Sci. **112**, 406 (2016).
[32] F. Peng, Y. Sun, C. J. Pickard, R. J. Needs, Q. Wu, and Y. Ma, Phys. Rev. Lett. **119**, 107001 (2017).
[33] C. J. Pickard and R. J. Needs, J. Phys.: Condens. Matter **23**, 053201 (2011).
[34] Z. M. Geballe, H. Liu, A. K. Mishra, M. Ahart, M. Somayazulu, Y. Meng, M. Baldini, and R. J. Hemley, Angew. Chem. Int. Ed. **57**, 688 (2018).
[35] A. Iyo, I. Hase, K. Kawashima, S. Ishida, H. Kito, N. Takeshita, K. Oka, H. Fujihisa, Y. Gotoh, Y. Yoshida, and H. Eisaki, Inorg. Chem. **56**, 8590 (2017).
[36] K. Momma and F. Izumi, J. Appl. Crystallogr. **44**, 1272 (2011).
[37] T. Fernique, A. Hashemi, and O. Sizova, Discrete Comput. Geom. (2020), doi:10.1007/s00454-019-00166-y.
[38] Three-dimensional data of densest binary sphere packings and our open-source program package SAMLAI (Structure search Alchemy for MateriaL Artificial Invention) are available at http://www.samlai-square.org.
[39] A. Togo and I. Tanaka, arXiv:1808.01590.
[40] H. Minkowski, *Geometrie der Zahlen* (Leipzig: Teubner, 1910).
[41] S. Vajda, *Mathematical Programming*, Dover Books on Computer Science Series (Dover Publications, 2009).